On the characterisation of photovoltaic device parameters using light beam induced current measurements.

Lucian John-Ross Bezuidenhout

Submitted in fulfilment of the requirements for the degree of

Magister Scientiae

in the Faculty of Science at the Nelson Mandela Metropolitan University

February 2014

Supervisor: Prof E.E. van Dyk

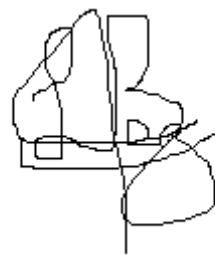Co-Supervisor: Dr F.J. Vorster

Co-Supervisor: Dr MC. Du Plessis

Declaration

Full Names: Lucian John-Ross Bezuidenhout

Student No: 207074356

Qualification: Magister Scientiae

In accordance with Rule G4.6.3, I hereby declare that the above-mentioned treatise/ dissertation/ thesis is my own work and that it has not previously been submitted for assessment to another University or for another qualification.

Lucian John-Ross Bezuidenhout

Dated: February 2014

This is dedicated to my parents Reginald and Julia Bezuidenhout

Acknowledgements

Abstract

Light Beam Induced Current (LBIC) measurement is a non-destructive technique used to perform localized characterization of solar cells using a light beam as a probe. The technique allows the determination of local photo response of a cell, the electrical parameters and defects that occur in the individual solar cell.

The semiconductor materials used to create solar cells are not always defect free and these defects reduce the electrical performance of the device. It is therefore important to use a system that will allow the characterization and extract the solar cell parameters as can be done using the LBIC system. By analysing these parameters and cell defects, further studies can be done to enhance the cell's lifetime and hence its efficiency. Light beam induced current (LBIC) is a technique that focuses light onto a solar cell device and thus creating a photo-generated current that can be measured in the external circuit for analyses. By scanning this beam probe across a solar cell while measuring the current-voltage characteristics, a map of various parameters can be obtained.

This thesis presents the design of the LBIC system, the software interfacing of the data acquisition system and local photo-response within different solar cell technologies. In addition, this thesis represent two curve fitting algorithms namely: the Gradient Descent Optimisation and the Differential Evolution used for the extraction of solar cell device parameters. The algorithms are based on the one-diode solar cell model and make use of the light generated current-voltage (I-V) data obtained from the LBIC system.

Different solar cell technologies namely; single crystalline (c-Si) and multicrystalline silicon (mc-Si) was used for analysis. LBIC maps and I-V characteristics of both technologies was obtained. The LBIC maps shows performance degrading defects present in the bulk and the surface of the solar cells as a function of spatial distribution. These localised defects acts as trapping mechanism for the charge carriers and therefore limits recombination within the solar cell and thus decreasing the performance of the solar cell device. The resulting I-V characteristics obtained from the LBIC system were used to determine the performance parameters using the two algorithms. The resultant effect of these parameters on the performance of the solar cells was observed.

The overall results showed that LBIC is a useful tool for identifying and characterising defects in solar cells.

Contents

List of Tables

List of Figures

Chapter 1: Introduction

The decrease in the availability of fossil fuels and the abundant availability of solar energy, makes photovoltaics reliable and a useful alternative energy resource. The sun can supply power up to approximately 1353 W/m^2, known as the solar constant. However, due to scattering and absorption of light from the earth's atmosphere this solar constant is reduces to approximately 832 W/m^2, which is still an abundant clean source of energy.

1.1   Non-uniformity in solar cells

The semiconductor materials used to manufacture solar cells are not always defect free [1]. These defects present in the material negatively impact the electrical performance of the solar cells. Standard characterisation tools such as visual inspection, electroluminescence and infrared thermography do not fully characterize the extent of performance limiting defects. To facilitate the characterization of the solar cells with respect to these defects, a light beam induced current measurement (*LBIC*) system that utilizes light as a beam probe to investigate point-by-point photo response may be used.

1.2   Objective of study

The objective of this study was to design and construct a Light Beam Induced Current (LBIC) system for the identification and characterization of performance degrading defects. LBIC is a technique that focuses light onto a solar cell device thus creating a photo-generated current that can be measured in the external circuit for analyses. By scanning this beam probe across a solar cell while measuring the current-voltage characteristics, a map of various parameters can be obtained. The primary purpose of this study was to create a device parameter extraction process that best approximates the solar cell device parameters. By extracting these device parameters the solar cell can be electrically characterised.

1.3   Outline

This section contains an overview and description of the chapters that follow.

Chapter 2 presents an introduction to the semiconductor principles and properties of solar cells. The formation of the different p-n junction and the effect of different biasing on the solar cell under illumination are discussed. The diode models used to describe the principle of the solar cell and the performance parameters extracted from the I-V characteristics of the solar cells are also discussed.

Chapter 3 discusses the different characterisation techniques with emphasis on LBIC. The principle of the LBIC scanning techniques and different measurements that can be obtained using this technique are discussed.

Chapter 4 focusses on the design and description of the constructed LBIC set-up. The purpose of each component is discussed in detail. In addition the two different configurations for the LBIC scanning are also described.

Chapter 5 discusses the two methods, gradient descent optimization algorithm and differential evolution used for the extraction of device and performance parameters from the illuminated I-V characteristics.

Chapter 6 discusses the results obtained from the LBIC system. The results show the LBIC maps for different solar cell technologies analysed namely; single-crystalline (c-Si) and multi-crystalline (mc-Si) silicon. In addition results from these solar cells when subjected to the parameter algorithms for electrical characterisation.

Chapter 7 gives an overall conclusion of the study.

Chapter 2: Principles of a Solar Cell

2.1   Introduction

The principle of solar cell operation is based on the photovoltaic (PV) effect, where an electron is excited to a higher energy level by a photon incident on a semiconductor material. When the photovoltaic device is connected to an external circuit, electrical power can be obtained.   This chapter discusses semiconductor properties and the models used to describe solar cells operation, the different types of solar cell technologies and the I-V characteristics associated with these devices. In addition, the influence of the device performance parameters will be discussed.

2.2   Semiconductor properties of a solar cell

A solar cell consists of a semiconductor diode, which is formed by joining *n*-type (with excess electrons) and *p*-type (with excess holes) semiconducting materials. The resulting *p-n* junction has an associated bandgap energy, E_g. When the solar cell is subjected to light, incoming photons which have energy equal to E_g, will excite the electrons from the valence band to the conduction band, leaving holes in the valance band. In the region of the *p-n* junction, an electric field will sweep the excess electrons to the *n* side of the junction, resulting in an excess of charge and thus an open circuit voltage (V_{oc}) can be measured. The energy of the incident photon is expressed as [1]:

$$E_\lambda = \frac{hc}{\lambda} \qquad\qquad (2.1)$$

where *h* is Planck's constant, *c* is the speed of light and *λ* is the wavelength of the incident photon.

Semiconductors are materials in which the range of excitation energies is interrupted by an energy bandgap between the valence and conduction bands. The allowed energy states per unit volume for certain energies above and below the bandgap energy are known as the density of states, *N(E)*. Figure 2.1 shows the energy states as a function of density of states.

The probability distribution function of the electrons with energy levels E within a semiconductor is given by the Fermi model, *f(E)* [2]:

$$f(E) = \frac{1}{e^{\frac{E-E_f}{kT}} + 1} \qquad\qquad (2.2)$$

where E_f, is the Fermi energy, *k* is the Boltzmann constant, and *T* is the temperature.

The Fermi model is strongly dependant on temperature [3] and indicates that at $T = 0$ K, all the states below the Fermi level are filled, and all those above the Fermi level are empty. With an increase in temperature, more energy states above the Fermi level will be occupied due to thermal excitation of the electrons to higher energy states.
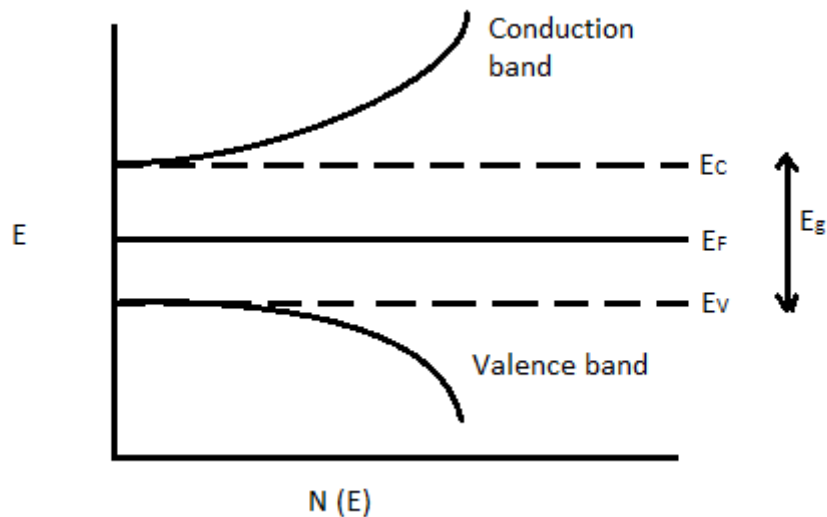
Figure 2.1: Energy bands in a semiconductor indicated by the density of states, N (E).

2.2.1 Mobile charge carriers

There are two main transport mechanisms that cause charge carriers to move through the semiconductor material, diffusion and drift. Diffusion occurs due to the difference in charge carrier concentrations between *p-* and *n*-type semiconductors. This concentration difference causes carriers to move from a region of higher concentration to a region of lower concentration in order to achieve equilibrium. Drift occurs when an external applied voltage is connected to the semiconductor device, and electrons are accelerated in a direction opposite to the internal electric field [4]. The crystallography of the semiconductor material negatively influence the drift velocity due to increase in collisions, where the mobility of the carriers is a function of the strength of the electric field, the level of the doping in the material and the temperature [4].

2.2.2 Homogeneous *p-n* junction model

A homogeneous *p-n* junction is one in which the *p*-type and *n*-type semiconductor is doped in such a way to form a single energy band E_g. The most common material used to form a homogeneous *p-n* junction, particularly in solar cell technologies, is silicon (Si) [5]. The properties of the energy bandgap of the material influence the efficiency of the solar cell, since photons with energy equal to the bandgap E_g will be absorbed for current generation. Photons with energy less than E_g make no contribution to current generation and those with an energy higher than E_g contribute to heating of the solar cell. The design of the *p-n* junction thus plays an important role in the performance of solar cells. The properties of the homogeneous *p-n* junction that influence the efficiency of a solar cell are the distribution of the dopants in the *p-* and *n*-sides of the semiconductor material, and the purity of the

semiconductor [1]. The thicknesses of the *p*- and *n*-layers also influence the efficiency of the device, since for good current generation the incoming photon should have a good penetration depth within the material [4].
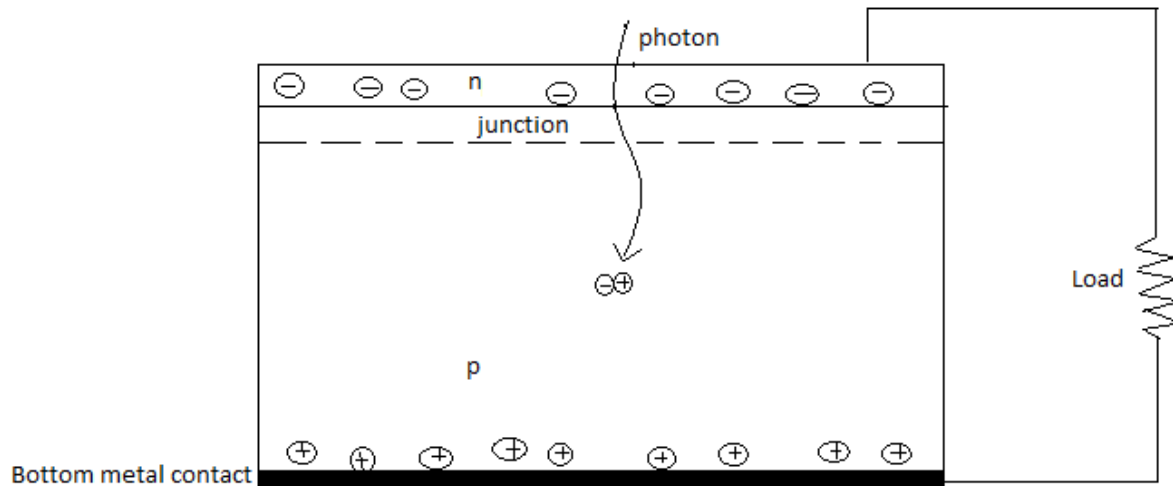
Figure 2.2: Homogeneous *p-n* junction structure connected to an external load.

Fig. 2.2 shows a homogeneous *p-n* junction under illumination connected to a load. The free movement of both electrons and holes allows for current generation in the semicondutor. When the solar cell is illuminated, electron-hole pairs are generated. Carrier collection occurs due to the diffusion of electrons (from *n*-type to *p*-type semiconductor regions) and holes (from *p*-type to *n*-type regions). When the homogeneous semiconductor is connected to an external load and the resulting junction is biased, the current-voltage (I-V) characteristics of the junction change.

a)   Zero bias / Thermal equilibrium

When the *p-n* junction is formed, a difference in the concentration of electrons and holes between the two semiconductors is created. This difference in concentration allows for free carriers in the *n*-region (e-) to diffuse across the junction to the *p*-region to combine with holes, and for holes in the *p*-side to diffuse across to the *n*-side. The transition region between the *n*- and *p*-type semiconductors is referred to as the depletion region [3]. Fig. 2.3 shows the enegry dagram of a *p-n* junction under zero bias. In order for current collection to occur, the lifetime of the charge carriers diffusing must be greater than their transit time towards the junction [6].
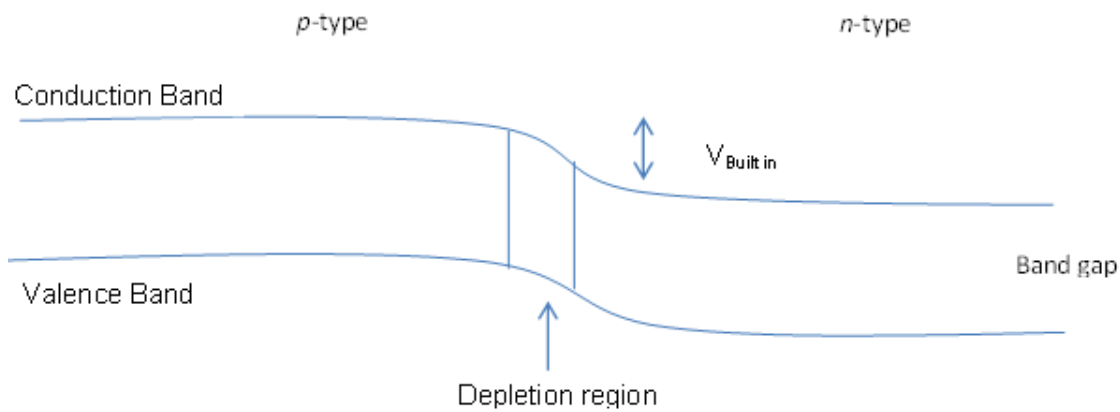
Figure 2.3: Energy diagram of a p-n junction at zero bias.

b)   Forward bias

Fig. 2.4 shows the enegry dagram of a *p-n* junction under forward bias. Forward biasing of the solar cell results in an electric field ($E_{built-in}$) which sweeps electrons from the *n*-side and holes from the *p*-side towards the *p-n* junction. The electric field (E_{load}) produced by the load is in the opposite direction to that produced by the diffused carriers. The net electric field thus consists of the built-in field (due to diffusion of carriers) minus the applied field, where $E_{built-in} > E_{load}$ [7]. The resulting depletion region is reduced and the diffusion barrier is lowered. The diffused carriers are the main contributors to current generation when the solar cell is forward biased, since the drift carriers are negligible. Fig. 2.5 shows an example of the I-V characteristics of an illuminated solar cell under forward bias.
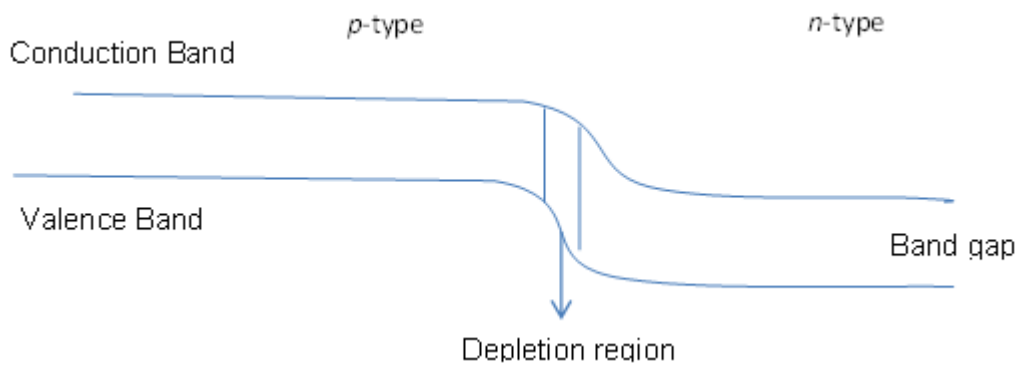
Figure 2.4: Energy diagram of a p-n junction subjected to forward biasing.
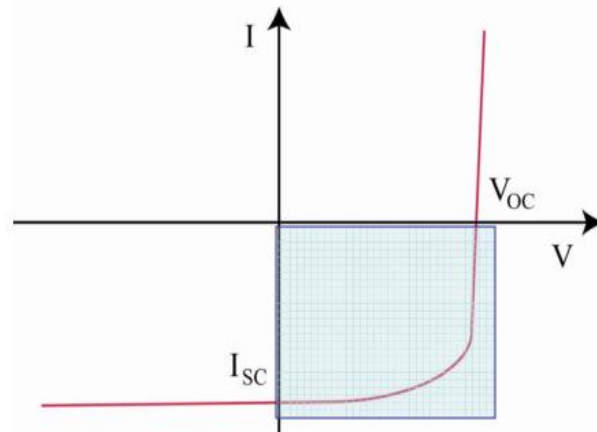
Figure 2.5: I-V characteristics of an illuminated solar cell under forward bias [8].

c)   *Reverse bias*

When the solar cell is reverse biased, there is a build up of the electric field at the *p-n* junction. The current measured under reverse bias occurs due to carriers generated by the illumination of the cell, since the higher electric field in the depletion region reduces the rate of diffusion across the junction, thus making the diffused current negligible. The drift current is a function of the number of minority carriers available within the material, and with an increase in drift current there is an increase in the depletion width of the solar cell.

Fig. 2.6 shows the enegry band diagrams of a *p-n* junction under reverse bias. The main contribution to current when a solar cell is reverse biased is drift current. The I-V characteristics of the junction under illumination are given in Fig. 2.7.
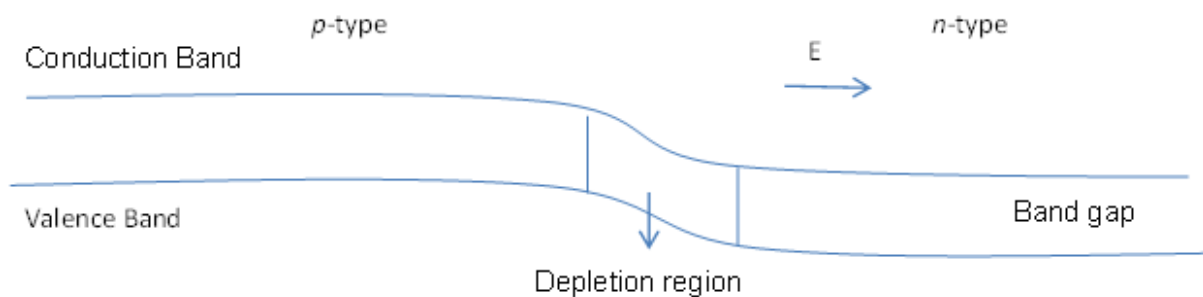
Figure 2.6: Energy diagram of a *p-n* junction under reverse bias.
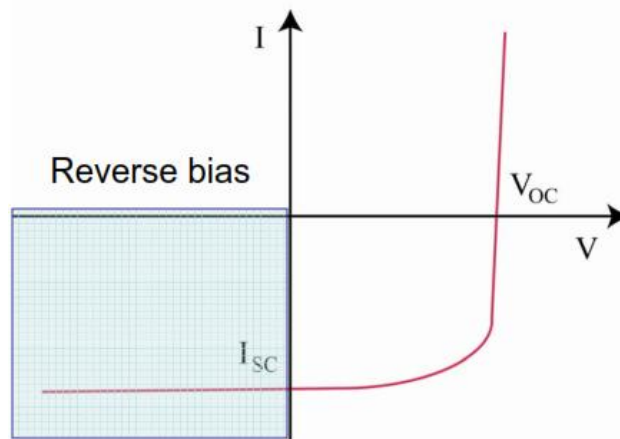
Figure 2.7: I-V characteristics of a solar cell under reverse bias during illumination [8].

2.2.3 Heterogeneous *p-n* junction model

Homogeneous band gap materials are most commonly used for solar cells; however there are other materials that can provide the desired I-V characteristics at lower costs and higher efficiencies [2]. Heterojunction solar cells are formed between semiconductors with different bandgaps. Multiple bandgaps connected in series allow for a wider absorption range of the solar spectrum, thus creating more carriers between the junctions. The most common heterojunction solar cells used in the PV industry are concentrator triple junction (CTJ) solar cells.

2.3 The diode models

Fig. 2.8 shows a schematic diagram of an ideal case equivalent circuit for a solar cell under illumination. The current (I) generated by the device is related to the load across the solar cell, the current across the diode, I_0, and the photo-generated current, I_L. The I-V characteristics for this case are expressed by eq. 2.3 [9]:

$$I = I_L - I_0 \left(exp^{\frac{qV_D}{kT}} - 1 \right) \tag{2.3}$$

The model does not take into account current losses due to the metallic contacts, shunt paths created by impurities present in the material, and the ideality factor (*n*), which is a property of the quality of the *p-n* junction which in most cases is assumed to be 1.
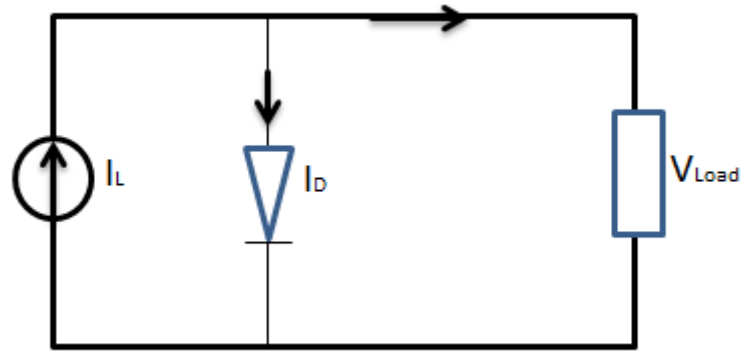
Figure 2.8: The equivalent circuit for an ideal solar cell.

This equation only assumes recombination routes between the bands of the semiconductor material [10]. For real cases, different recombination processes must be taken into account, which results in a change in the ideality factor. In the next section the diode model is altered to take into account the parasitic resistances and the quality of the diode.

2.3.1 The one-diode model

The equivalent circuit for a one diode solar cell which includes parasitic resistances can be modelled by eq. 2.4:

$$I = I_L - I_0 \left(exp^{\frac{q(V+IR_S)}{nkT}} - 1 \right) - \frac{(V+IR_S)}{R_{sh}} \tag{2.4}$$

where I_0 is the ideal saturation current, n is the diode ideality factor, I_L is the illuminated current, R_s is the series resistance, R_{sh} is the shunt resistance and T is the temperature. This equation is derived from the equivalent circuit model shown in Fig. 2.9, where the additional parasitic resistances (R_s and R_{sh}) are added to the circuit.

To accurately explain the I-V characteristics of a solar cell, the contribution of the parasitic resistances is taken into account. The current losses due to the metallic contacts (Ohmic losses) are referred to as the series resistance, and this reduces the voltage (= IR_s) produced by the cell, which in turn reduces the performance of the solar cell.
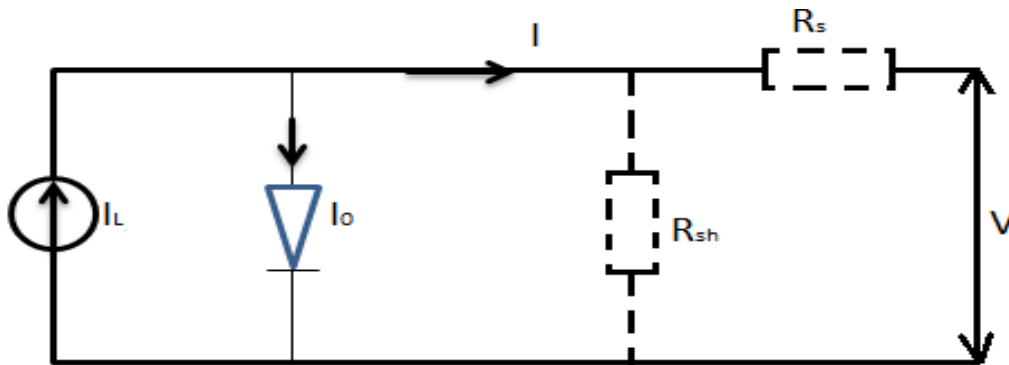
Figure 2.9: The equivalent circuit of a solar cell that includes the parasitic resistances R_s and R_{sh}.

The parallel shunt resistance is caused by impurities within the material which produce shunt paths that give rise to a shunt current (I_{sh}) that leads current away from its intended target, thus negatively affecting the performance of the cells [11]. For a good solar cell, R_{sh} must be infinitely large so that I_{sh} is negligible.

The one-diode model is used to extract the solar cell device parameters and will be discussed further in Chapter 5.

2.3.2 The two-diode model
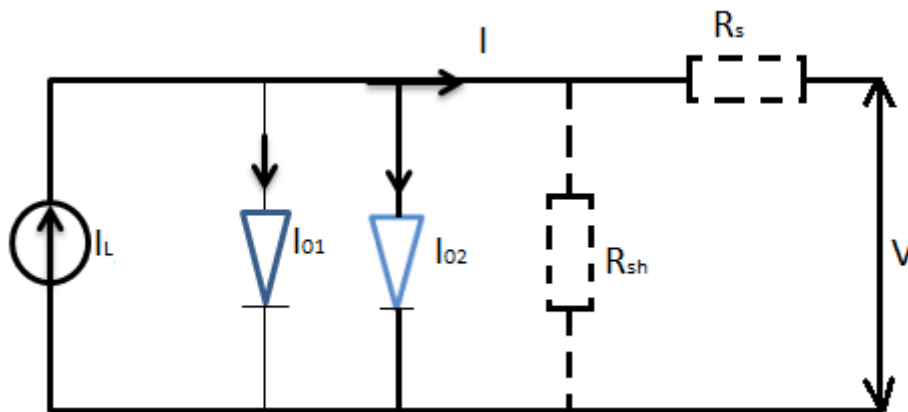
Figure 2.10: Equivalent circuit for the two-diode model.

As mentioned in the previous section, the model only assumes recombination routes between the bands of the semiconductor material. Since recombination effects can be detrimental to the I-V characteristics of the solar cell, they must also be accounted for. The two-diode model factors in the different types of recombination processes. The configuration of the equivalent circuit used to derive the equation for the two-diode model is shown in Fig. 2.10 and the equation is given by eq. 2.5 [10]:

$$I = I_L - I_{01}\left(exp^{\frac{q(V+IR_S)}{n_1 kT}} - 1\right) - I_{02}\left(exp^{\frac{q(V+IR_S)}{n_2 kT}} - 1\right) - \frac{(V+IR_S)}{R_{sh}} \qquad (2.5)$$

where I_{01} is the ideal saturation current, I_{02} is the non-ideal saturation current, n_1 and n_2 are the diode ideality factors, I_L is the illuminated current and T is the temperature. Each diode within the model has different saturation currents and ideality factors. The model is the only way of looking at n_1 and n_2 respectively.

2.4 Recombination processes

Recombination processes play an important role in the I-V characteristics of solar cells. The different types of recombination processes that occur within the semiconductor are shown in the schematic diagram in Fig. 2.11.
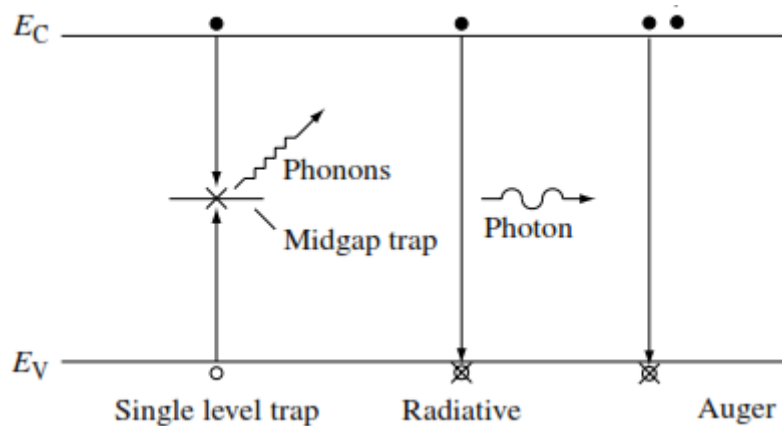
Figure 2.11: Recombination processes within the semiconductor [1].

2.4.1 Shockley-Read Hall / Trapping recombination

The impurities in the crystal structure give rise to new energy states, also known as traps, within the semiconductor material. These allow electrons and holes to recombine.

2.4.2 Radiative recombination

Radiative, or band to band recombination, is the reverse process of optical generation. The electron drops to a lower energy state to recombine with a hole and emits energy in the form of a photon.

2.4.3 Auger recombination

Auger recombination is similar to radiative recombination. However, the excess energy is not released as a photon, but is transferred to another carrier in either the valence or conduction band. After a period, the carrier loses its energy through thermal vibrations [1].

2.5   Device performance parameters

The diode models described in the previous section consist of a current source, one or two diodes and device parameters, namely shunt resistance (R_{sh}), series resistance (R_s), ideality factor (n) and saturated current (I_0). These parameters greatly affect the I-V characteristics of the solar cell and hence the performance of the PV device, and may be extracted from the light I-V curve [3]. A simulation of the diode equation with respect to a random set of I-V data was carried out and the effect of changing the parameters on the I-V characteristics was observed.

2.5.1   Parasitic resistances

From the diode equation, the relationship between the increase and decrease of these parasitic current loss mechanisms can be derived. From the one-diode model it can be seen that the series resistance (R_s) has no effect on the open circuit voltage, since current flows throughout the entire solar cell. However, short circuit current is affected. This is clearly seen in the simulation shown in Fig. 2.12.

The presence of shunt resistance (R_{sh}) is mainly due to manufacturing defects. Shunting provides alternative current paths for the light generated current, such divergence reduces the current flow through the p-n junction and reduces the voltage of the solar cell [11]. This effect is clearly seen in the I-V characteristic shown in Fig. 2.13.

The main contributors to these current losses are the emitter and base of the solar cell, metal contacts, and impurities induced by the semiconductor material.
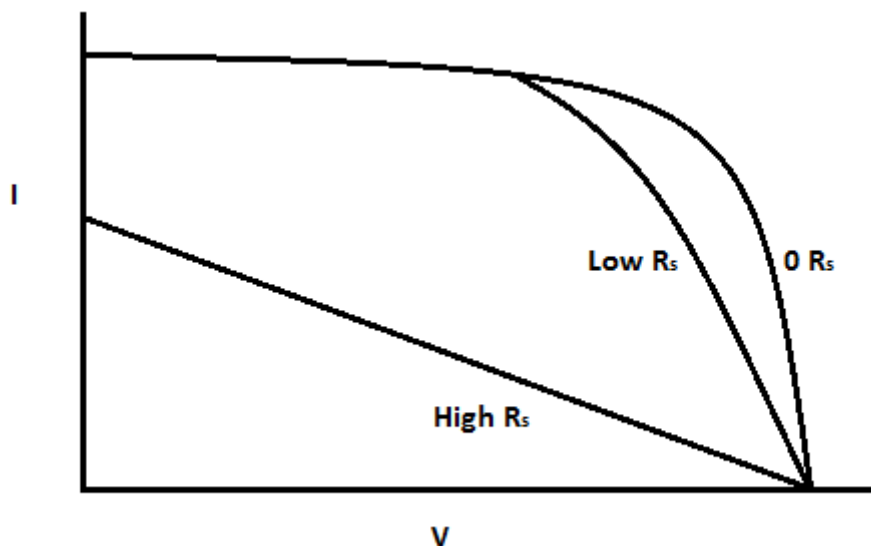
Figure 2.12: The effect of varying series resistance on the current-voltage characteristics.
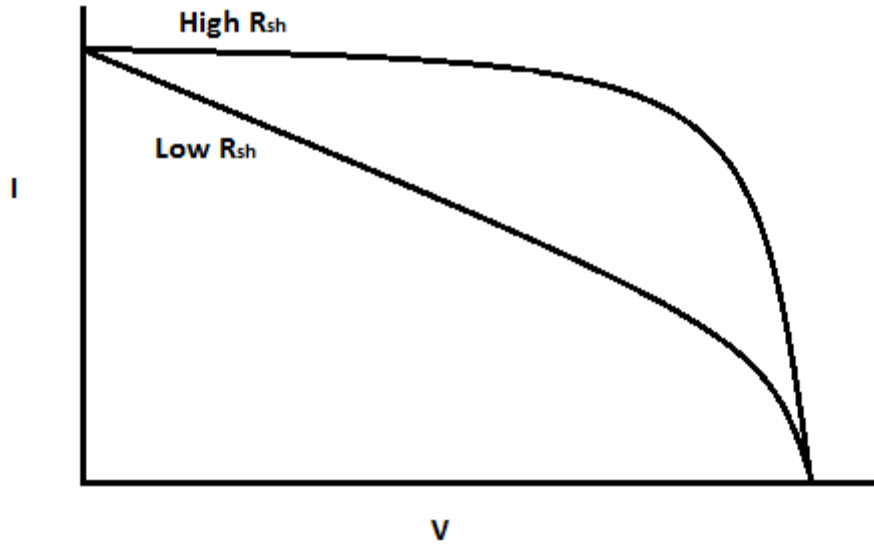
Figure 2.13: The effect of varying shunt resistance on the current-voltage characteristics.

2.5.2 Ideality factor

In the ideal case, the shunt resistance is assumed to be infinite and the solar cell model becomes:

$$I = I_L - I_{01}\left(exp^{\frac{q(V+IR_S)}{n_1 kT}} - 1\right) \tag{2.6}$$

The ideality factor *n*, which typically ranges between 1 and 2, is a measure of how closely the diode follows the diode equation and is influenced by the different recombination states [1]. An ideality factor of n = 1 occurs due to band-to-band recombination, n = 2 is due to recombination taking place in the junction, and 1 < n < 2 occurs due to a combination of all the recombination processes. The ideality factor typically influences the "knee" of the I-V curve and its effect can be seen in Fig. 2.14.
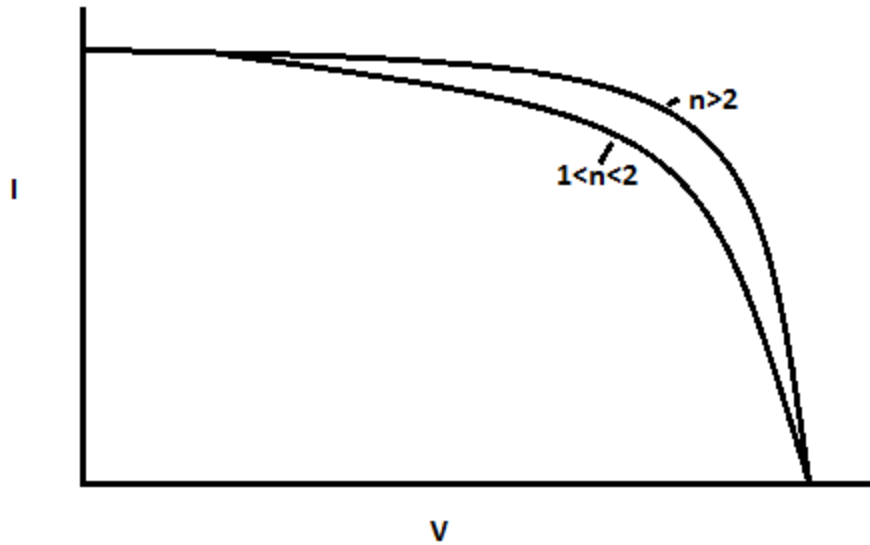
Figure 2.14: The effect of a variation of the ideality factor on the current-voltage characteristics.

2.5.3 Light generated current

The illuminated current, I_L, is independent of the voltage across the cell and is sometimes assumed to be the short-circuit current (I_{sc}), since it depends solely on the photons incident on the solar cell [11]. This is a good approximation, since at small voltages the diode current and other parameters are negligible. With this assumption in mind, the light generated current can easily be found on the I-V curve and diode equation when V = 0.

2.5.4 Open circuit voltage

Like I_L, the open circuit voltage (V_{oc}) can be easily retrieved from the I-V characteristics at I = 0 and can be expressed as [8]:

$$V_{oc} = \frac{k_B T}{q} \ln\left(\frac{I_{sc}}{I_0}\right) \qquad (2.7)$$

2.5.5 Fill factor

The fill factor (*FF*) is a measure of the deviation of a real solar cell from the ideal, and is expressed as the ratio of the maximum power output (P_{max}) to the product of I_{sc} and V_{oc} [3]:

$$FF = \frac{P_{max}}{I_{sc} V_{oc}} \qquad (2.8)$$

14

2.5.6 Efficiency

Efficiency (η) is defined as the ratio of power output to the power input:

$$\eta = \frac{P_{max}}{EA} \qquad (2.9)$$

where E is the irradiance incident on the solar cell and A is the area of the cell.

The performance parameters were extracted using the one-diode model discussed in section 2.2.1, by means of the gradient descent and differential evolution algorithms. A detailed description of these model-fitting techniques will be discussed in Chapter 5.

2.6 Solar cell structure

A conventional solar cell consists of a p-type wafer which forms the bulk of the device and a very thin n-type layer on the surface of the solar cell known as the emitter. Fig. 2.15 shows the structure of a conventional solar cell. Under illumination, the electric field draws electrons to the emitter of the solar cell and holes to the base. The metallic mesh (contacts) situated on the surfaces of the solar cell allow for the collection of the charge carriers, which are then carried to an external load [10]. An anti-reflection coating (ARC) is placed on the surface of the solar cell to minimise reflection and allow maximum illumination of the solar cells.
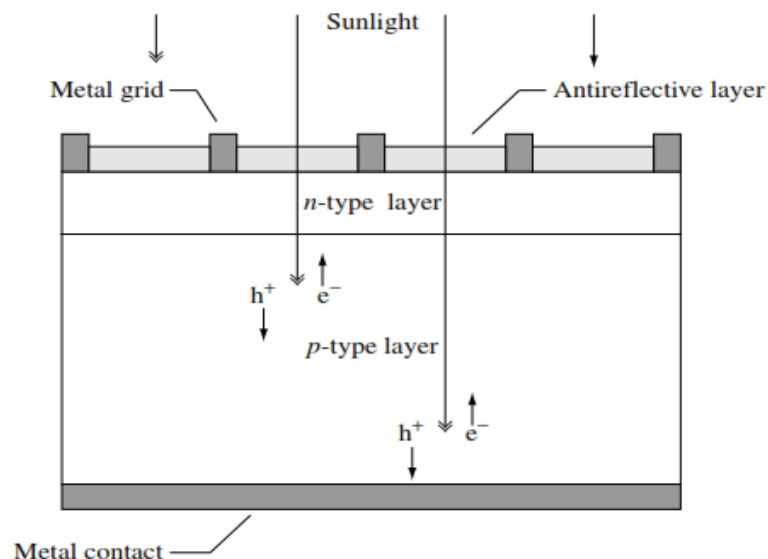
Figure 2.15: Structure of a conventional solar cell indicating electron-hole separation [1].

2.7   Solar cell materials

The most common semiconductor material used is silicon (Si), due to its periodic crystal structure, the number of valence electrons available to form covalent bonds and its absorption characteristics, which is a fairly good match to the solar spectrum.   Other semiconductor materials used for the manufacture of thin-film solar cells will not be discussed as they were not part of this study.   The typical spectral response of a Si solar cell, which is the ratio of the current carriers within the solar cell to the power incident on the cell, ranges from 300 nm to 1200 nm [12].   Photons with energy greater than that of the bandgap are strongly absorbed by the solar cells, however these photon energy are wasted, since the electrons thermalize back down quickly to the conduction band edges [13]. Photons that do not have enough energy to excite the electrons will interact weakly with the semiconductor and will pass through the material as if it was transparent.   Photons with energy equal to the bandgap have just enough energy to create an electron-hole pair for current generation.

2.8   Summary

Solar cells were described in terms of a *p-n* junction, where the *p*-region is heavily doped with holes and the *n*-region with electrons.   The operation of *p-n* junctions with a single bandgap under different bias conditions was discussed.   The models describing the I-V characteristics of the solar cell were derived and the effect of the parasitic resistances and possible recombination processes on the solar cell model were identified.   The solar cell device parameters were defined and their effect on the light I-V characteristics was described using a simulation.   The one-diode equation will be used to extract the device parameters using the gradient descent and differential evolution algorithms, and will be discussed further in Chapter 5.   In addition a brief description of the solar cell structure and materials used were also discussed.

Chapter 3: Characterisation Techniques

3.1 Introduction

Most photovoltaic technologies make use of silicon to form the solar cells. However, its high cost and scarcity have resulted in the more regular use of different types of materials due to their low cost and higher throughput [13]. Due to the non-uniformity of the crystal structure within these materials, trapping mechanisms for the photo-generated current are enhanced and hence the recombination processes within the solar cell are reduced, which results in a decrease in solar cell efficiency. The impurities within the different crystal structures reduce the performance of the device, and it is therefore critical to have a non-destructive method of identifying and characterising the performance parameters.

Standard characterisation tools, such as visual inspection, electroluminescence, infrared imaging etc, act as complementary techniques to characterise the extent of these performance limiting defects. Light Beam Induced Current (LBIC) is a non-destructive technique that focuses light onto a solar cell device, inducing a photo-generated current that can be measured as a function of its position on the cell surface. By measuring the variation in the photo-generated current as the beam probe is scanned across the cell, the performance limiting defects can be identified and therefore characterised. This chapter discusses the principle of LBIC and a brief description of other characterisation techniques is also provided.

3.2 Monochromatic current generation

The photo-current generated by a monochromatic wavelength incident on a solar cell is a function of the excitation of the charge carriers within the n- and p-regions and the space charge region (SCR). Therefore, the total current (I) generated at a given wavelength λ is expressed as [7]:

$$I(\lambda) = I_n(\lambda) + I_p(\lambda) + I_{SCR}(\lambda) \tag{3.1}$$

where $I_n(\lambda)$ = the photo-generated current in the n-region

$I_p(\lambda)$ = the photo-generated current in the n-region

$I_{SCR}(\lambda)$ = the photo-generated current in the space charge / depletion region

3.3 Light Beam Induced Current (LBIC)

The total efficiency of a photovoltaic device depends on the efficiency at each point on the solar cell. Scanning techniques such as LBIC allow for the identification and characterisation of defects as a function of spatial distribution within the solar cell. LBIC generally uses a monochromatic laser beam as a beam probe to inject photons onto the surface of a solar

cell. Multiple wavelength laser probes are commonly used for the characterisation of concentrator triple junction solar cells [14]. By illuminating the solar cell and scanning in a raster pattern while measuring the photocurrent signal as a function of position, a photo-response map indicating the performance degrading defects in the solar cell can be obtained. The photo-generated current is restricted by the interaction of electrons and other carriers produced by grain boundaries and defects present in the semiconducting material. This trapping mechanism influences the carrier generation and recombination states of the solar cell [7] and therefore decreases the efficiency of the device. The principle of the LBIC technique is visually explained by Fig. 3.1.
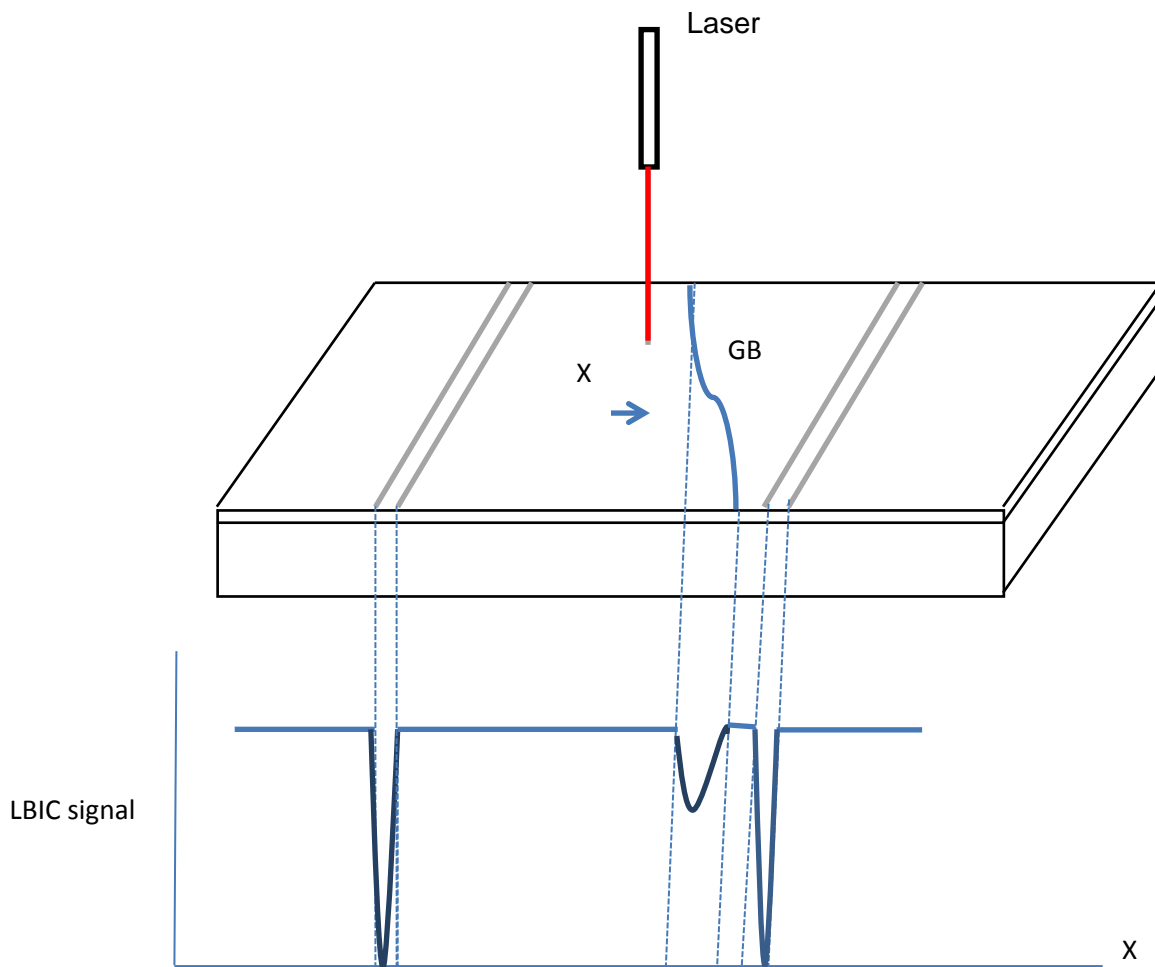
Figure 3.1: LBIC signal configuration as the laser is scanned across the solar cell.

The LBIC signal contains information about the properties of the solar cell under illumination. The signal gives a direct relationship between the photocurrent produced at a point and an identification of a reduction in the photo-generated current and therefore the identification of the spatial defect present in the cell. Figure 3.1 shows the LBIC signal configuration indicating the scanning direction (*x*) and the effect of a grain boundary (*GB)* on the LBIC signal as the laser is scanned across it.

3.4   Line scans

By scanning the light beam across one axis and keeping the other axis constant a line scan across the solar cell can be obtained at different bias voltages. Line scans are commonly used to provide information about the LBIC signal level at different bias voltages and to determine the beam diameter, which will be discussed in the next section. Fig. 3.2 shows an example of line scans of the same region, obtained at different biases, for a multi-crystalline silicon solar cell. The decrease in current due to shading by the cell's contact fingers is clearly shown. The lines present below I_{sc} represent the scan taken at reverse bias voltages while the lines above indicate scans obtained at forward bias. The extent of the current reducing defects and their effects on the photo-generated current at different bias voltages can also be clearly seen. The induced current measured at the contact fingers is fairly constant indicating that the shading effect caused by the metal contacts is fairly constant across the cell. The current loss mechanisms measured at the defects under different bias conditions are different, and this is indicative of the different recombination and localised shunting effects occurring in these regions [10].
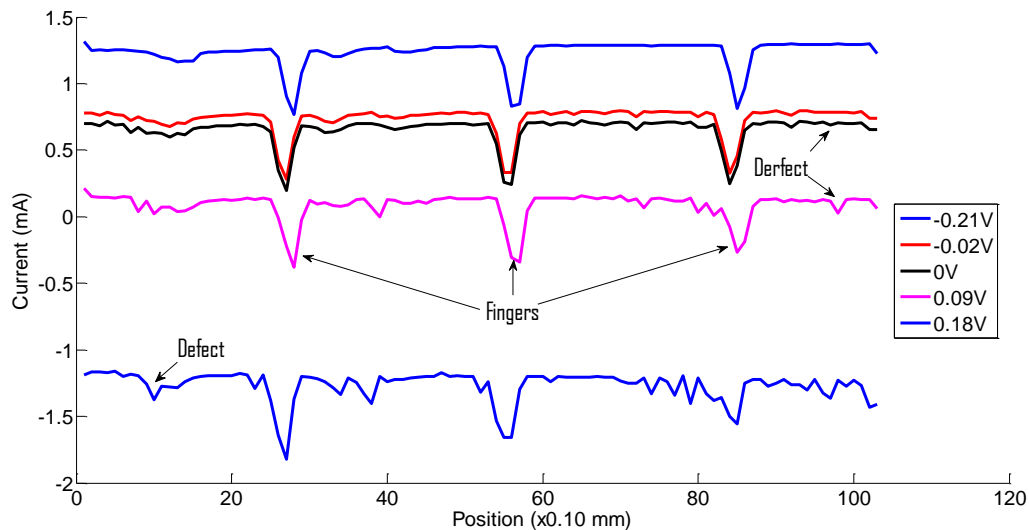
Figure 3.2:   Line scans cross the multi-crystalline Si solar cells at different biasing voltages.

3.5   System characterisation

3.5.1   Resolution

LBIC measurements depend on the resolution of the scan and the wavelength of the incident light, since enough energy is required to excite the charge carriers within the device. Factors influencing resolution are beam spot size, beam intensity and the step size between each point.

a) Beam spot size
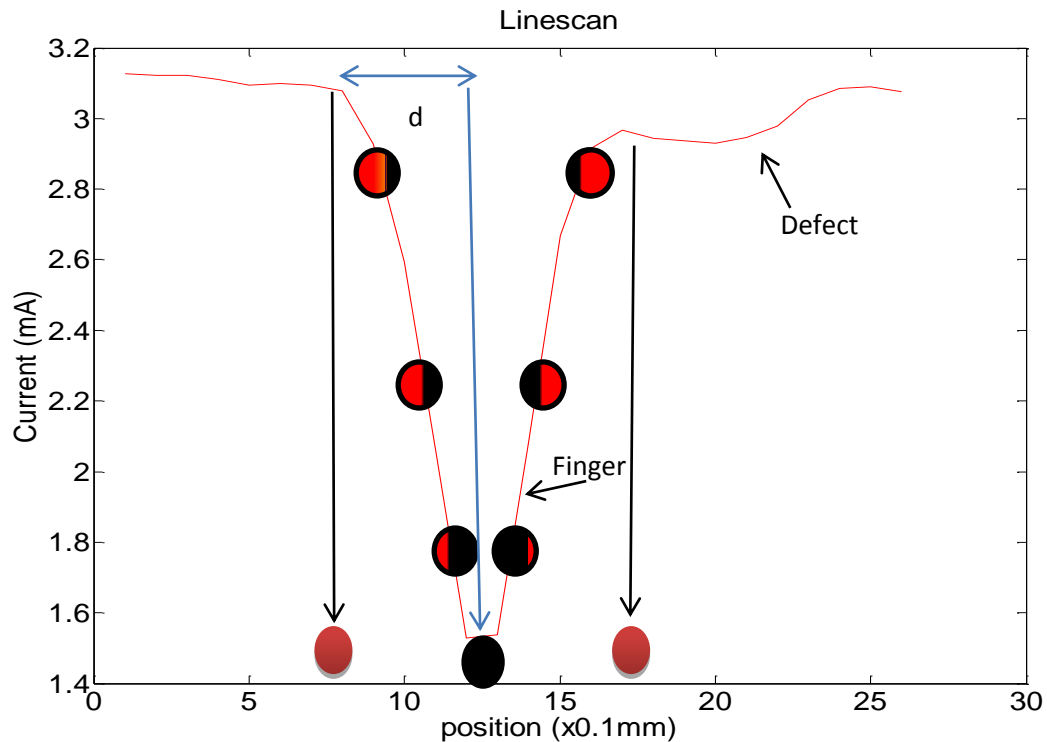
Figure 3.3: Line scans cross the single-crystalline Si solar cells indicating the variation of the beam across a finger.

The spot size of the beam can be varied by using optical equipment. The change in beam diameter does not significantly change the intensity of the beam, but increases the exposure area of the light incident on the solar cell [9]. Fig. 3.3 shows a line scan across the contact finger of a single crystalline Si solar cell. The beam diameter is determined by measuring the distance from where the beam starts scanning over the edge of the finger to where the LBIC signal is lowest over that finger, since it is between these regions that the beam is totally incident on the finger. The figure clearly indicates the model of the beam as its moving across the finger.

b) Beam intensity

The beam intensity is varied with interface software that controls the power of the laser and is discussed in Chapter 4. The intensity of the beam incident on the solar cell is a function of the optical path and the diffraction of the laser beam. The higher the intensity of the beam, the more carriers are excited within the solar cells, since there is a proportional relationship between the current produced by the cell and beam intensity. A variation in the beam intensity could lead to some local areas within the cell performing less well than other local areas. It is thus important to keep the beam intensity constant for accurate measurements.

3.5.2 Bias voltage

The LBIC system also allows for the sample to be placed under both forward and reverse bias by using an alternating current voltage source (waveform generator). At pre-determined bias voltages, the photo-generated current is measured, which allows for the generation of I-V curves and subsequent device parameter extraction. The performance of the solar cell can thus be evaluated, and this will be discussed in later chapters.

3.5.3 Photo-response / Surface scanning.

By illuminating the cell and scanning in a raster pattern while measuring the electrical signal at each point, a two or three dimensional map can be constructed. Each surface map indicates the electrical performance of the solar cell at different bias voltages. The surface map indicates the extent and inhomogeneity of the current reducing features as a function of position on the solar cell. Fig. 3.4 shows an example of a surface and photo-response map for a single crystalline silicon (c-Si) solar cell. The scan clearly shows the contact fingers and other current reducing features. The fingers acts as shading features and therefore no current is generated in these regions [7]. The scan also reveals a scratch across the solar cell surface, which probably occurred due to poor handling of the cell. Additional current reducing defects, shown by the arrows, could be due to impurities present in the semiconductor material that could have been introduced during the manufacturing processes.
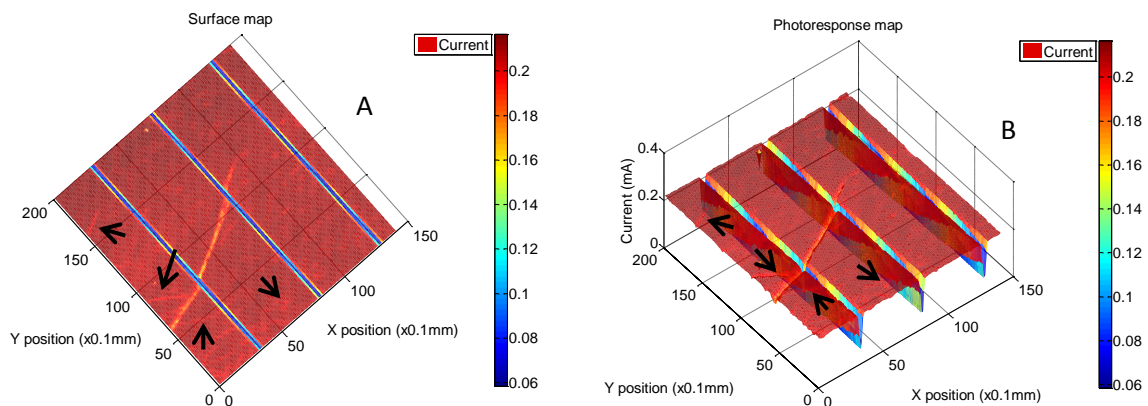
Figure 3.4: (a) Surface map and (b) Photo-response map of a c-Si solar cell.

3.6 Electroluminescence

Electroluminescence (EL) can be used as a complementary technique for identifying damaged or cracked cells. The technique is based on injecting free carriers into the junction by forward biasing the solar cell. Radiative recombination of carriers causes the emission of energy in the form of a photon, and this can be captured as electroluminescence with a Si-CCD camera. The intensity of the EL signal is a function of the inherent material, thus defects influencing the recombination process are seen in the fluctuation of the EL signal and these can be identified [10]. EL is a much faster technique than LBIC, however, it does not characterise device performance in a quantitative manner.

3.7 Summary

The Light Beam Induced Current technique is a non-destructive diagnostic tool used to identify and characterise performance degrading defects in solar cells. In this chapter, the principle of LBIC was discussed and the system resolution was briefly explained in terms of beam spot size and intensity. Line scans indicating the contact fingers and other current reducing defects were obtained at different bias voltages, indicating the extent of these defects on the generated current signal. A description of surface and photo-response maps was briefly introduced and will form the basis of the analysis procedure in later chapters.

Chapter 4: Experimental Details

4.1   Introduction

The LBIC technique was used in this investigation to study the defects present in semiconductor devices and to characterise the devices in terms of the parameters extracted from their I-V curves.   The technique is based on shining a light beam onto the semiconductor device and measuring the point–by-point electrical activity present within the sample.   This chapter details the LBIC and I-V measurement systems designed and constructed for this study. In addition, each component of the system and its contribution to the LBIC measurements are discussed. The LBIC system designed allows for flexibility so that different experiments can be carried out.

4.2   LBIC measurement system

4.2.1   Set-up

Fig. 4.1 is a schematic diagram of the LBIC system designed and constructed for this study. The system consists of a laser source for current generation at each point, a beam expander, an aperture, an objective lens, an x-y stage driven by stepper motors, and a PID temperature controller.   The sample is illuminated by a 633 nm wavelength laser beam, where the 50/50 beam splitter directs the beam perpendicularly onto the sample under investigation.
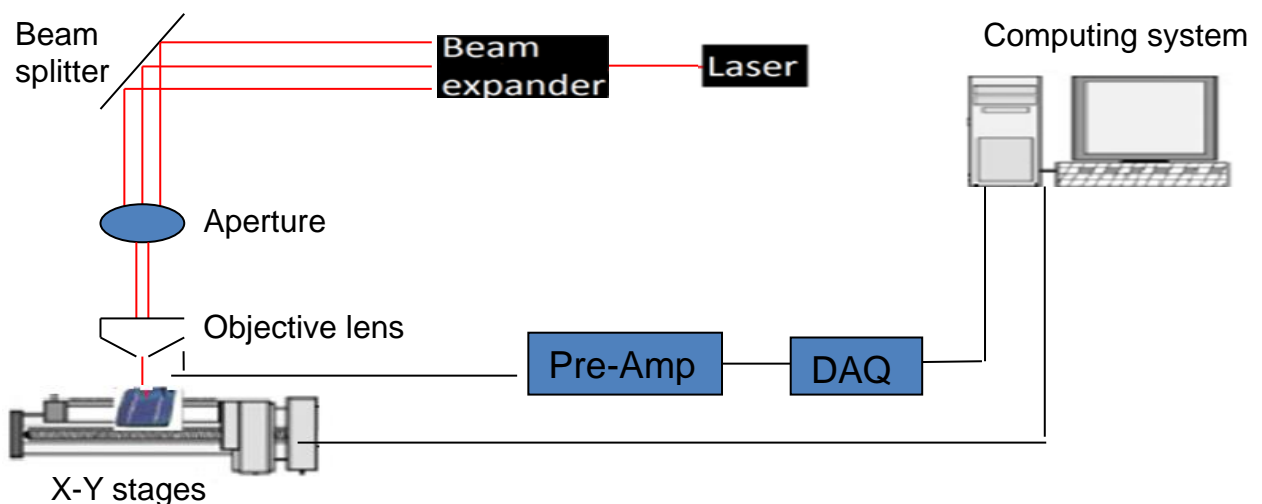
Figure 4.1:   Schematic of the LBIC system designed.

The adjustable aperture in front of the objective lens allows for variation of the diameter of the beam focused on the sample. A Labview programme was written to interface the data acquisition systems (DAQ in Fig. 4.1) and the x-y translation stages. The system also allows

for variation of the wavelength, since the sample is fixed to the scanning system and the laser source is interchangeable. In addition, the Peltier cell allows for the temperature of the system to be controlled. A photograph of the constructed LBIC system is presented in Fig. 4.2, and shows all the components depicted by Fig. 4.1.
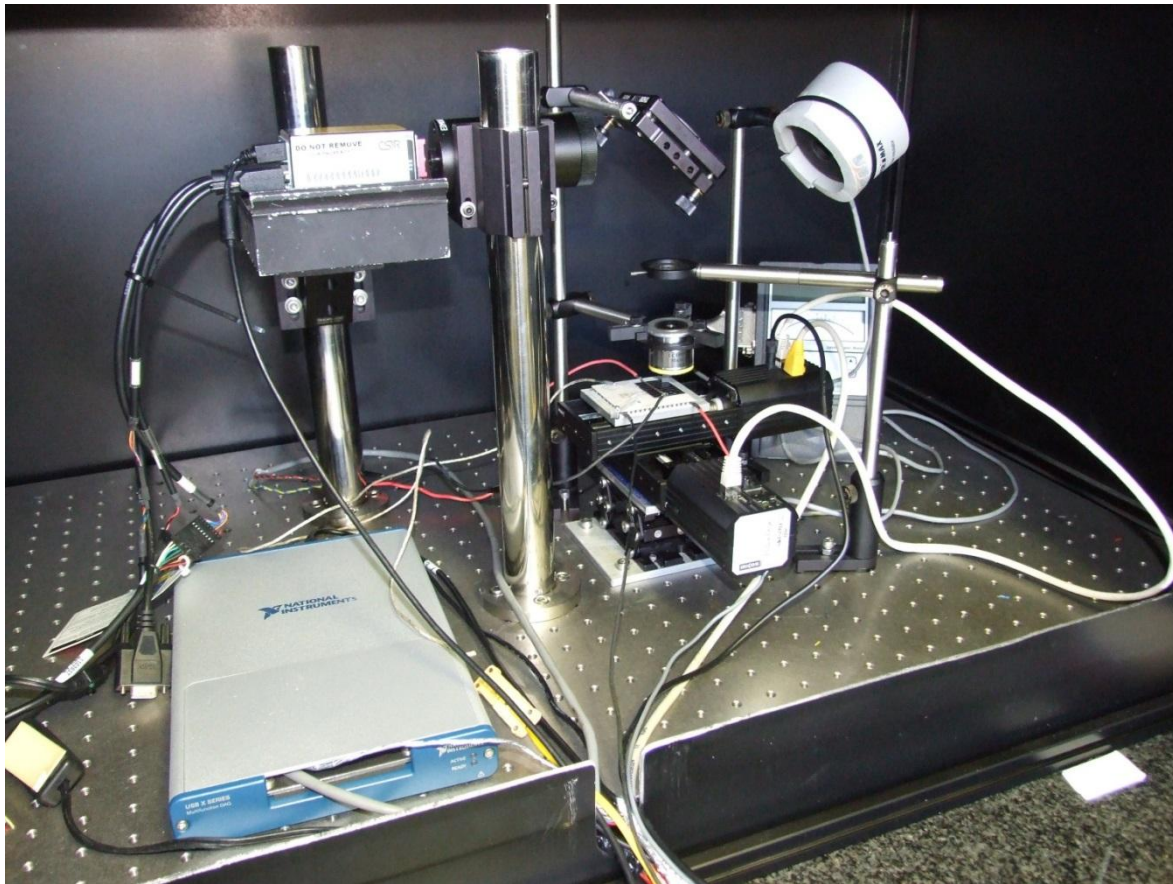
Figure 4.2: Photograph of the LBIC system.

Current is generated when the solar cell under investigation is illuminated by the monochromatic laser source. Before the LBIC scan begins, the interface software requires inputs such as the scan area, selection of the voltage interval, the desired scanning routine and scanning step size for the desired resolution. The cell is then scanned in a raster pattern under illumination, and the current is measured and amplified by the pre-amplifier, which converts the amplified current to a voltage. This voltage is then transferred to the data acquisition system (DAQ). The DAQ converts the analogue signal to a digital signal which is analysed by the computing system. The system is enclosed within a metal enclosure to facilitate a dark environment and to shield from external electromagnetic radiation which may interfere with the acquired LBIC signal.

4.3   Point-by-point I-V measurements

4.3.1   Set-up

While the LBIC system can measure photo-response, as discussed in the previous section, it also allows for point-by-point I-V measurements of the solar cell. By forward and reverse biasing the cell with a programmable alternating current voltage source (waveform generator) while scanning the cell under illumination, the I-V characteristic of each point on

the cell can be obtained. This allows for device parameter extraction and hence characterisation of the performance of the solar cell device. Figure 4.3 indicates a schematic of the I-V measurement system, in addition to the LBIC system the I-V measurement configuration is just an addition of the waveform generator for biasing of the solar cell. The measuring principle is similar to that discussed in the previous section. The only difference is that the induced current is measured and amplified at predetermined voltages. For analysis, a LabView programme was written to plot current and voltage as a function of position on the solar cell.
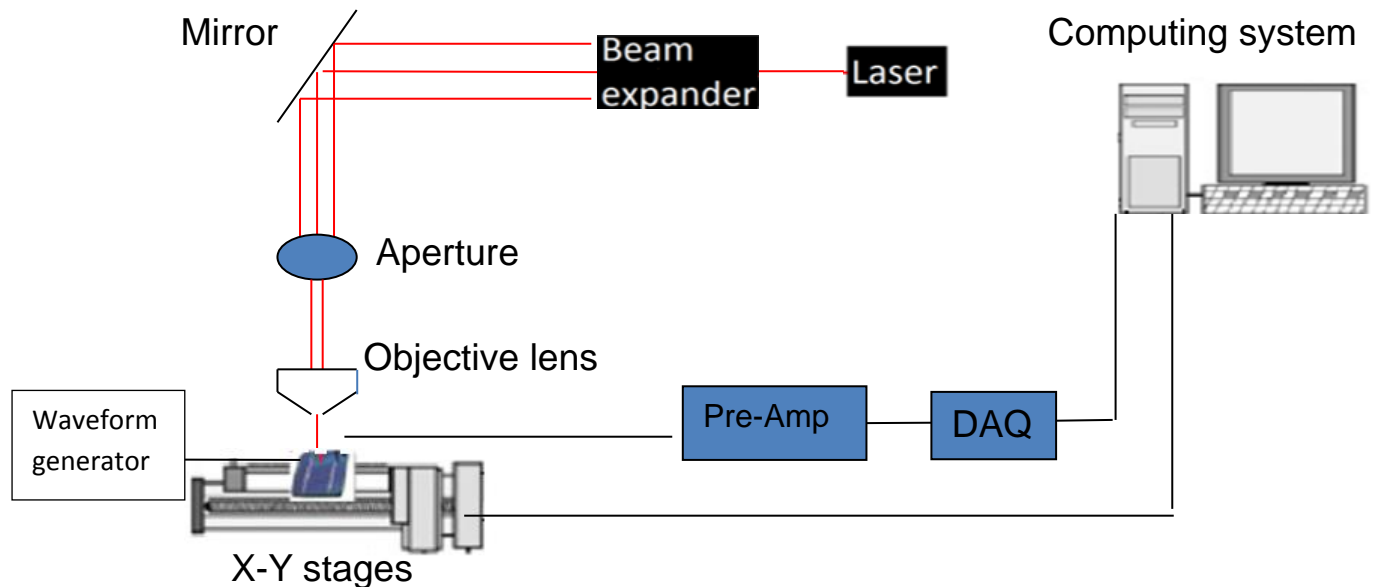
Figure 4.3: Schematic of the I-V system designed.

4.4   Components

The following section discusses the apparatus used for the LBIC and IV measurements.

4.4.1   Laser source

The 633 nm monochromatic wavelength laser source used to illuminate the solar cells for LBIC and I-V measurements is shown in Fig. 4.4. The Coherent cube laser is mounted on a heat sink to dissipate heat produced while lasing. The cube laser produces a beam in the intensity range, 1 mW – 60 mW. In addition, the laser has a warm-up time of less than 5 min and a base plate temperature ranging between 10 and 50 °C. Laser beam parameters such as beam intensity and mode status (i.e. pulse or analogue) are controlled by the computer using integrated software and RS-232 or USB connections.
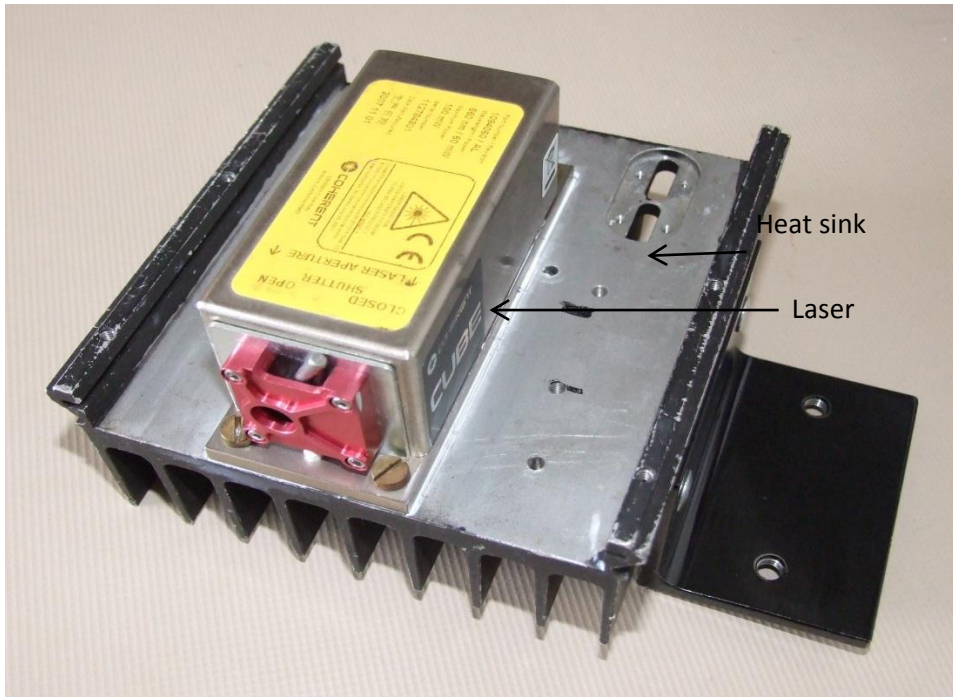
Figure 4.4: Coherent cube 660 laser source with heat sink.

4.4.2   Beam Expander

Fig. 4.5 shows a picture of the 6x beam expander used for LBIC and I-V measurements. The beam expander increases the diameter of an input collimated beam to a larger collimated output beam. The beam diameter of the incident light is increased and diverges onto an achromatic lens, which results in the beam being collimated. The diameter of the resultant expanded beam is varied by the adjustable ring in front of the expander [15].

Figure 4.5: 6X beam expander.

4.4.3　Reflective mirror

The mirror used for reflecting the laser beam perpendicular to the solar cell sample is shown in Fig. 4.6.
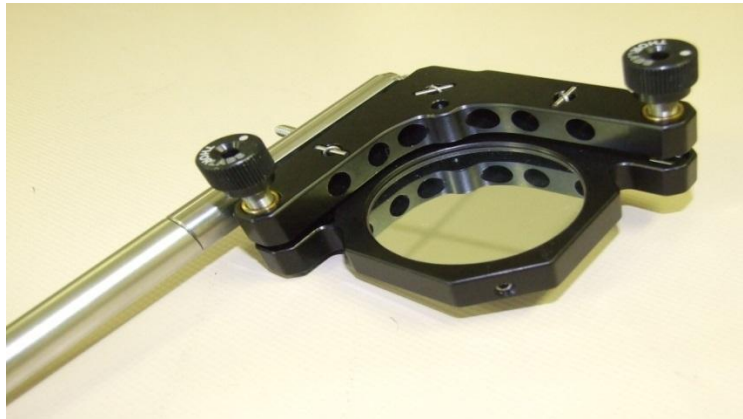
Figure 4.6:　Reflective mirror.

4.4.4　Aperture

The aperture is placed in front of the objective lens for further collimation of the incident beam and to decrease the diameter of the beam incident on the objective lens. The lever on the side of the aperture allows one to set the desired cone angle and the amount of rays allowed through. Fig. 4.7 shows a picture of the aperture used in this investigation.

 Figure 4.7:　Aperture.

4.4.5　Objective lens

Fig. 4.8 shows the objective lens used to focus the laser beam incident onto the solar cell in order to increase the resolution of the system. The EC "Epiplan" objective lens provided by Zeiss optics has a 10x magnification and a working distance of 14.3 mm. The incoming beam is reflected off of small mirrors inside the objective and is reflected back by a concave mirror to the exit of the objective where the beam is focused.

Figure 4.8: Photograph of objective lens.

4.4.6 X-Y stages and stepper motors

The point-by point movement of the solar cell placed on a sample holder is controlled by X-Y stages and stepper motors. These are shown in the photograph in Fig. 4.9. The two linear stages with the stepper motors are serially interfaced to a PC and controlled using a LabView programme. The stepper motors have a velocity range of 0.1 µm/s to 40mm/s and allow for high resolution scanning. The maximum linear resolution is 1 nm [16].
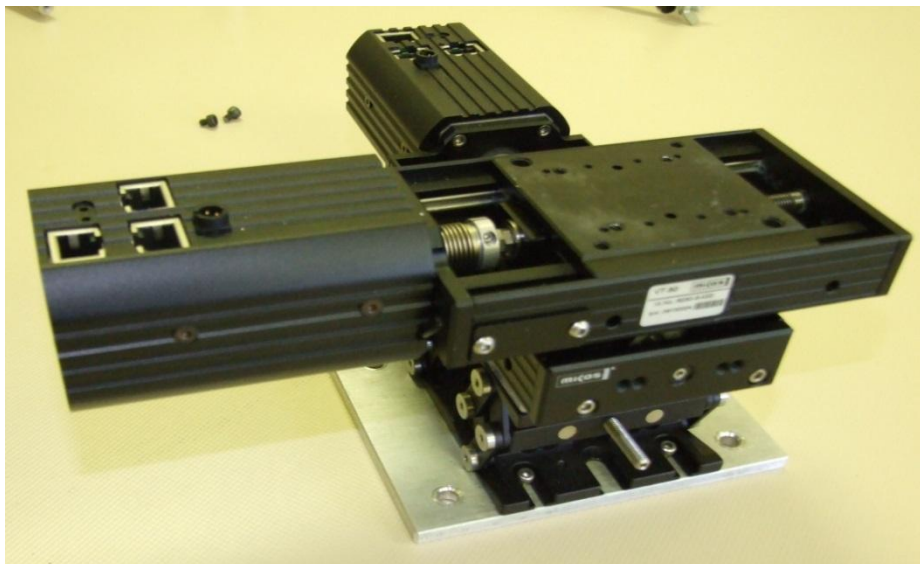
Figure 4.9: X-Y stages with stepper motors

4.5 Data acquisition

4.5.1 Current pre-amplifier

An SR570 low noise current pre-amplifier was used to amplify the LBIC signal sent to the DAQ. The amplifier takes an input current signal and converts it into an output voltage signal. The front panel of the pre-amplifier is shown in Fig. 4.10, and allows for the variation of input parameters such as sensitivity settings, filter type and bias voltage [17]. The sensitivity ranges from 1 pA/V to 1 mA/V. The induced current from the solar cell is measured by an insulated Bayonet-Neill-Concelman-connector (BNC) and is connected to the current pre-amplifier input, where it is converted to a proportional voltage. The SR570 allows for a DC current offset to supress any background current signals at the input. The

offset range varies from 1 pA to 5 mA in distinct increments [17]. The output voltage from the pre-amplifier is transferred to the data acquisition system via a BNC.

Figure 4.10: SR570 pre-amplifier used for signal amplification.

4.5.2 Waveform generator

Figure 4.11 shows the Agilent 33220A alternating waveform generator used for reverse and forward biasing of the solar cell. The Agilent allows for a range of waveforms, but for this study a sine waveform was chosen with a frequency range between 1 µHz and 20 MHz and a resolution of 1 µHz. The waveform generator is interfaced with a PC via a GPIB cable, where the parameters of the input wave are controlled.

Figure 4.11:   Agilent 33220A waveform generator used for biasing of the solar cell.

4.5.3   The data acquisition system

Figure 4.12:   National Instruments data acquisition system.

The National Instruments USB-6356 data acquisition system (DAQ) converts the analogue data signals to digital signals before transferring it to the PC for analysis. The USB-6356 consists of 16 simultaneous analogue inputs with a 16-bit resolution and a sample rate of 1.25 MS/s per channel [18]. The DAQ simultaneously measures the current induced in the solar cell and the voltage applied across the cell. A LabView programme was written to interface the current and voltage measurements and the positioning, which allows for current-voltage characteristics of the solar cell under investigation to be obtained.

4.5.4   System software

The system software consists of a LabView programme written to control the X-Y stages and stepper motors which move to a desired scanning position, and to synchronise the position with the current and voltage measurements obtained from the DAQ system.   The programme allows the user to specify the scanning area on the cell, the scanning step size, the bias voltage interval and the scanning routine, i.e. 2-D maps (line scans) or 3-D maps (surface scans).   After scanning is complete, the programme allows for movement and zooming of the maps in order to make rapid identification of defects within the solar cells. In addition, the programme allows for the capturing of current and voltage values as a function of position on the solar cell, which allows for point-by-point current-voltage characteristics.

4.6   Temperature control: the Peltier cell
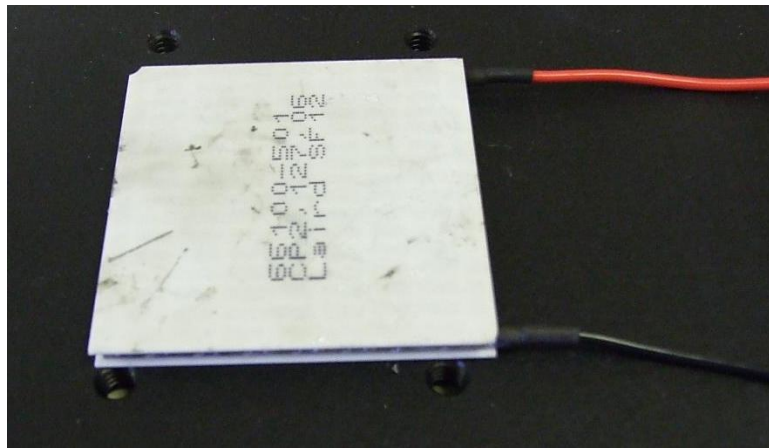
Figure 4.13: Peltier module.

A Peltier module is made out of an alternating arrangement of dissimilar junctions (*p*- and *n*-type) and one is shown in Fig. 4.13. When a DC voltage is applied over the module, the majority carriers of the two junctions move in the same direction, resulting in the heating of one side and the cooling of the other side of the Peltier. If the polarity is changed the reverse happens. A heat sink is pasted onto the hot side of the Peltier for heat dissipation. A Peltier module is a good way to control the temperature of the solar cell: by placing a thermocouple on the back of the cell and controlling the current supply, the desired temperature can be obtained.

4.7   Summary

This chapter discussed the design, construction and the components of the LBIC system used for this study. The LBIC system constructed allows for the qualitative analysis of solar cells using photo-response, line scans and point-to-point I-V characteristics, which in turn allows for the identification and characterisation of defects present in the solar cell. In addition, the system also allows for the regulation of the temperature of the solar cell by means of a Peltier module. The LBIC system was used to analyse solar cells fabricated using different cell technologies, and the results obtained are discussed in Chapter 6.

Chapter 5: Parameter extraction

5.1   Introduction

The working of a solar cell is described in terms of the one and two diode models [1] as discussed in Chapter 2. The models describe the current generated by the solar cell device in terms of the load across the cell, the current in the diode, the photo-generated current, the current losses due to parasitic resistances and the quality of the semiconductor diode [2]. The I-V characteristics obtained from these models allow for the extraction of the device performance parameters using numerical curve-fitting optimisation techniques.

This chapter gives a brief introduction of the optimisation process and discusses the two device parameter extraction algorithms that were used as complimentary techniques for parameter extraction: a gradient-descent optimisation algorithm and a differential evolution algorithm.   The parameters extracted from these algorithms are used to describe the electrical behaviour of the solar cells.

5.2   Optimisation

Optimisation refers to the process where the optimal solution to a given problem, known as an optimisation problem, for some available range is obtained. It consists of minimization or maximization of some objective function by steadily choosing an input value for an allowed set and computing the max or min value. In the case of this study the objective function was the one-diode equation, given by eq. 5.1, where the device parameters are to be minimized or maximized. Optimization of these parameters allows for the electrical characterisation of the solar cells being studied.

5.3   Gradient-descent parameter extraction algorithm

In the ideal case, the one-diode model is expressed by equation 5.1 as discussed in chapter 2, where the current I generated by the solar cell is described as a function of the device performance parameters ($n, I_0, R_s, R_{sh} I_L$):

$$I = I_{L-} I_0 \left(exp^{\frac{q(V+IR_S)}{nkT}} - 1 \right) - \frac{(V+IR_S)}{R_{sh}} \tag{5.1}$$

The device parameters that describes the quality of the device are extracted from the model by means of a technique called the gradient-descent method. The method makes use of the area under the light I-V curve and the I-V curve generated by the diode equation for an initial approximation for each device parameter.   The area *A*, shown in Fig. 5.1, is minimised with respect to each variable by taking the half sum square error between the data I-V curve and model I-V curve. The model can thus be expressed as shown in figure 5.1 and equation 5.2.
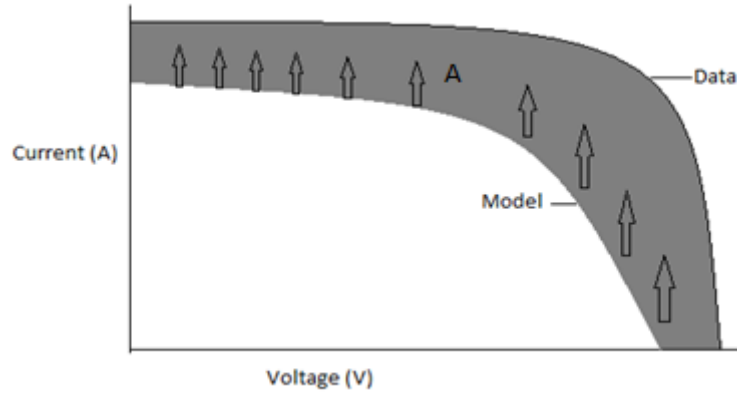
Figure 5.1: Parameter extraction model.

The resulting model is expressed as:

$$I\big(area(x)\big) = \frac{1}{2}\Sigma\big(I(data) - I(model(x))\big)^{2} \qquad (5.2)$$

where $x = [n, R_s, R_{sh}, I_o, I_L]$.

To minimise the half sum squared error function with respect to each parameter, the best fit model was obtained by setting the derivative of the difference between the data and the model, given by equation 5.2 to zero:

$$\frac{dI}{dx} = 0 \qquad (5.3)$$

The roots of the resulting integral are determined using the gradient-descent optimisation method. This is an iterative numerical method. For a given differential function and initial point/guess (x_o), it follows the negative of the gradient and iteratively moves the initial guess in the direction of the negative gradient in order to get the desired local minimum X_{x_o} [23]. The gradient-descent method is given as:

$$X_{x_o} = x_o - \varepsilon\frac{dI}{dx} \qquad (5.4)$$

where eta (ε) is the locally optimised step size and differs for each parameter being optimised, and is a function of the convergence rate of each parameter. Each parameter was optimised individually and thus the partial derivative with respect to each parameter was taken for the optimisation process. The gradient-descent iteration was repeated several times for each point on the solar cell to allow smooth convergence of the parameter. A flow chart of the gradient-descent optimisation algorithm is shown in Fig. 5.2 and is a summary of the optimisation process.
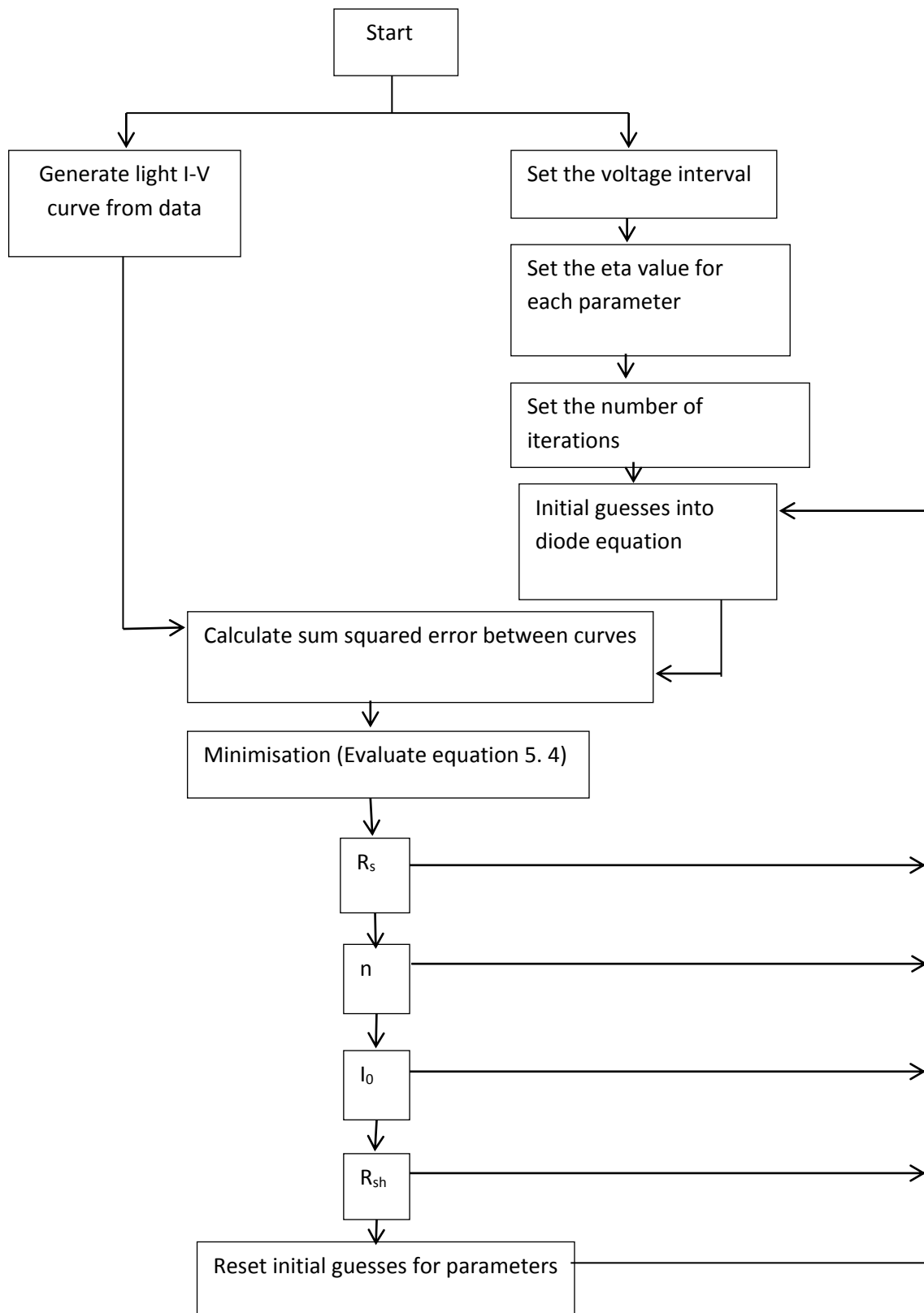
Figure 5.2: Flowchart of the one-diode gradient descent parameter extraction optimisation model.

When starting the optimisation process, the data received from the LBIC system is used to generate the light I-V curve. Before running the algorithm initial parameters and limitations on the algorithm, such as; the voltage interval used, the initial guess and eta values for each parameter are set. In addition to this the number of iteration for each optimisation process was fixed. The initial guesses are set into the diode model and the I-V curves are obtained. The sum squared error between the data and the model was calculated before minimisation took place. After the evaluation of equation 5.4, the initial guesses are refined and the algorithm continues with this process till convergence is obtained.

The method yields a good approximation for n, I_0, R_s and R_{sh}. Initially, the model considered two assumptions: firstly, I_L was approximated to be I_{sc}. This is a fairly good approximation since the Illumination current depends entirely on the incoming photons incident on the solar cell and is independent of the voltage across the cell [11]. The second assumption made is an infinitely large R_{sh}, which is expected for the ideal case. However, this assumption was later removed from the model. During this optimisation process, it was observed that different combinations of these parameters fit the I-V characteristics of the solar cell, and there could thus be a slight accuracy offset due to this combination factor.

To observe this combination effect that the parameters have on each other and on the I-V characteristics of the solar cell, the diode model was differentiated with respect to each parameter. The resulting derivatives are indicated by equations 5.5 – 5.8:

$$\frac{dI}{dR_s} = \frac{-I_0 I q}{nkT} \, e^{\frac{q(V+IR_S)}{nkT}} - \frac{I}{R_{sh}} \tag{5.5}$$

$$\frac{dI}{dn} = \frac{I_0 q(V+IR_S)}{n^2 kT} \, e^{\frac{q(V+IR_S)}{nkT}} \tag{5.6}$$

$$\frac{dI}{dI_0} = - \, e^{\frac{q(V+IR_S)}{nkT}} + 1 \tag{5.7}$$

$$\frac{dI}{dR_{sh}} = \frac{(V+IR_S)}{R_{sh}^2} \tag{5.8}$$

The low voltage region of the I-V curve is mainly dependant on the shunt resistance (R_{sh}), the knee of the curve depends largely on the ideality factor (n), and the high voltage region depends on the series resistance (R_s). However, considering the change in the diode equation with respect to each parameter, it is evident that for dramatic changes or high values of R_s, I_0, n and R_{sh}, will affect the different region of the I-V curve. This result indicates that when fitting the curve using some model, different combinations for the extracted parameters could fit the same curve and thus there is a degree of uncertainty in the modelled values of the extracted parameters.

5.3.1 Computing time

The time dependence of the parameter extraction algorithm is mainly a function of the minimisation of the area between the data and model (equation 5.2). Initially, Newton's method was used to obtain the roots for this function; however, this was very time consuming when running the algorithm for multiple points on the solar cell. In order to obtain a faster convergence for this function, Newton's method was replaced by the gradient-descent method, which allows for a faster convergence, but is heavily dependent on the ε value for each parameter and the number of iterations at each point. The ε value is chosen by trial and error. By running the algorithm for less iterations for a given ε value, a plot of the convergence was obtained and this allowed for the verification of a good ε value. If a good, precise ε value is chosen, the algorithm converges smoothly and quickly.

5.3.2 Accuracy of the model

The accuracy of the model was calculated using the square of the difference between the current values obtained from the data and the current values obtained from the fit. This indicates the deviation of the model from the actual data set and is given by the following equation:

$$SS= \sum (I_{data} - I_{model})^2 \qquad (5.9)$$

5.4 Differential evolution method

5.4.1 Evolutionary computing

Evolutionary computing is an optimisation technique based on the principle of biological evolution [24]. This technique is widely applied to a variety of problems, ranging from practical applications in the industry and scientific research. The population of the possible solutions are iteratively evolved by increasing the reproduction of better fit solutions. Differential evolution is a sub branch of Evolutionary computing and is known to be an effective optimisation algorithm in static environments and will be discussed in the next section.

5.4.2 Differential evolution scheme

Differential evolution (DE) is used as a complementary technique to the gradient-descent optimisation algorithm for the extraction of device performance parameters. DE is known to be a reliable, accurate, robust, easy to use and fast optimisation technique and was created by Storm and Price in 1996 [19]. It is a stochastic population-based direct search algorithm that solves objective functions that are non-linear, non-differentiable, non-continuous and have multiple local minima. The general problem formulation for differential evolution is described as:

Suppose we want to optimise a function with D real parameters, in this case the parameters being optimised are the solar cell device parameters, where the parameter vectors have the following form:

$$\boldsymbol{X_i} = [X_{1,i}, X_{2,i}, \ldots\ldots, X_{D,i,}] \qquad\qquad i = 1, 2, 3, \ldots\ldots N$$

where N is the size of the population [19].

The general solution to the evolutionary procedure is shown in Fig. 5.3.
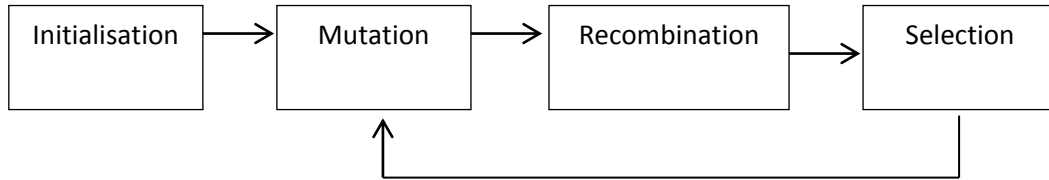
Figure 5.3: General evolutionary procedure.

The initialisation steps set the upper and lower boundaries for each parameter:

$$X_J^L \leq X_i \leq X_J^U$$

where X_J^L is the lower limit and X_J^U is the upper limit for each parameter and is chosen on prior knowledge on the range of values that each parameter can be a subset of.

In addition to the boundary conditions being set, initial values for each parameter (x_0) are randomly selected uniformly on the intervals:

x_0 subset of $[X_J^L, X_J^U]$.

The next step, mutation, expands the search space, so that for a given parameter vector $\boldsymbol{X_i}$, the algorithm randomly selects three distinct vectors $\boldsymbol{x_{i\,1}}$, $\boldsymbol{x_{i\,2}}$, $\boldsymbol{x_{i\,3}}$ and creates a new mutant vector, $\boldsymbol{v_i}$, using [19]:

$$\boldsymbol{v_i,} = \boldsymbol{x_{i\,1}} + F(\boldsymbol{x_{i\,2}} - \boldsymbol{x_{i\,3}})$$

where F lies between $(0, \infty)$.

The main idea behind generating the mutant vector is by adding the weighted difference vector between two population members to a third member, if the subsequent vector yields a lower objective function value than a predetermined population member, the newly determined vector replaces the vector with which it was compared with [19].

The $rand_{j,I} \sim U[0,1]$ recombination section of the algorithm consists of the incorporation of successful solutions from the previous generation. It creates a trail vector, $\boldsymbol{u_{ij}}$ from elements of the mutant vector with a probability of Cr as follows:

37

$$u_{i,j} = \begin{cases} u_{i,j}, & \text{if } U[0,1] \leq Cr \text{ or } j = r \\ \\ x_{ij} & \text{otherwise} \end{cases}$$

where Cr є (0, ∞) is the crossover probability and r is a randomly selected index [20].

The last segment of the differential evolution algorithm is selection criteria. In this section the mutant vector (v_i), and initial guess (x_i) is compared. The one which equates to the lowest SSE function value, in this case the error between the data obtained from the LBIC system and the one diode-model, is admitted to the next generation. The algorithm computes:

$$x_i = \begin{cases} u_{i1} \text{ if } f(u_i) \leq f(x_i) \\ \\ x_{i,} & \text{otherwise.} \end{cases}$$

The mutation, recombination and selection process continues until some criteria is met, which is normally the number of iteration for each parameter being optimized. For a detailed description of the DE scheme, see du Plessis *et al.* (2012) [20].

5.5 Differential evolution control parameters

Other than the parameters presented by the differential scheme, the DE has other control parameters such as the population size (n_l), scale factor (F) and the crossover factor (Cr) that needs to be set.

5.5.1 Scale factor (F)

The scale factor controls the size of the difference vector, and thus the amount by which the base vector, also known as the initial guess, is changed. Large values of F leads to a large scale exploration of the fitness landscape and this leads to premature convergence. Premature convergence can result in the transition from exploration to exploitation too early [20]. Small ranges of F result in a more detailed exploration of the local fitness landscape, but increases the convergence time.

5.5.2 Crossover factor (Cr)

The crossover factor controls the variety of the population space. Large values for Cr result in a large exploration of the fitness landscape, which may result in slow convergence. Conversely, small values of Cr lead to premature convergence. Therefore, a value for Cr must be chosen in such a way that it is large enough to ensure sufficient exploration and small enough to allow fast convergence. Reliable combinations for F and Cr are available in the literature, however, optimum results in terms of convergence and accuracy are obtained if the parameters are set for each problem individually [20].

5.5.3   Population size (n_I)

Like the crossover factor, the population size influences the diversity of the population. In addition to this, it also controls the number of function calculations performed per iteration. A large population size results in a more diverse sampling of the search space. A respectable value for n_I is one that is chosen to ensure a satisfactory number of iterations, but also allows for a sufficient exploration of the fitness landscape.

5.6   Differential evolution applied to the one-diode model

The one-diode model, discussed in Chapter 2, is a non-linear model that is not easy to differentiate.   The DE model described above was applied to this model where the parameters being optimized were n, I_0, R_s, R_{sh}. A fairly small scale factor of $F = 0.3$ was used, and this allows for a detailed exploration of the local fitness landscape. A crossover factor of $Cr = 0.6$ was used, and this allowed for a larger variety in the population. This combination of F and Cr allows for a fairly accurate optimisation and fast convergence time. Several changes to the DE process discussed above were made to make optimisation of the parameters easier. These changes included, using a different fitness function to allow for a smoother fit of the turning point on the graphs, this was done by taking the weighted errors between the successive points. One of the main changes made, was to optimise each parameters for each point on the solar cell parallel. During the optimization process, the DE algorithm used information not only from the population of the current point, but also from points directly around the current point. This process allowed for information about the optimal parameters to be shared amongst the parallel DE algorithm.

5.7   Summary

This chapter discussed the two models used to extract device parameters from the light I-V characteristics of solar cells. The models used the one-diode model to extract the parameters. The principle gradient-descent optimisation algorithm minimises the area between the light I-V curves obtained from the data and the model, and optimises that minimisation. The differential evolution algorithm is a stochastic population-based search algorithm which makes use of a large search space of solutions and mutates its way to the optimum solution.

Chapter 6: Results and Discussions

6.1   Introduction

This chapter presents the results obtained using the LBIC measurement system discussed in Chapter 4. It discusses the defects present within the solar cells that cannot be observed visually and have a deleterious effect on the performance of the cells. LBIC and I-V characteristics of two different solar cell technologies, single crystalline (c-Si) and multi-crystalline (mc-Si) silicon, were obtained. The I-V characteristics were used to obtain device performance parameter maps of the solar cells using gradient-descent optimisation and differential evolution algorithms, as discussed in Chapter 5. In addition, the effect of temperature on the performance of the solar cell was observed by obtaining LBIC maps at different temperatures.

6.2   LBIC analysis of single crystalline silicon solar cells

Single crystalline silicon solar cells were used for this analysis. LBIC measurements were carried out using a 633 nm wavelength laser beam with a spot size incident on the cells of approximately 80 μm, and a 100 μm step size. The smaller the beam spot size the better the resolution of the LBIC maps. LBIC current maps depict the current distribution across the solar cell and the I-V characteristics allow for the extraction of the performance parameters. Figures 6.1 and 6.2 show LBIC maps for a 15 x 15 mm^2 c-Si solar cell at 22°C and 46°C, respectively. The scans clearly show the contact fingers and other current-reducing features, which are indicated by the arrows. The light incident on the metallized fingers and bus bars is reflected due to the inherent reflection properties of metals. As a result of this shading no current is generated in these regions [1]. Current losses occur due to the geometry of the contact fingers and because the spot size diameter is greater than the width of the fingers. This loss is due to the shadowing of the incident light on the edges of the fingers. It has been reported that contact fingers shadow between 3 and 12 percent of the incident light [21]. Localised shadowing results in heating, since the shadowed region becomes reverse biased, which degrades the performance of the cell.

Current losses near contact fingers and bus bars are mainly attributed to Ohmic losses, where the metallization of the contacts induce impurities within the materials, and these defect centres act as trapping sites for carriers reducing the photo-generated current, which results in a decrease in solar cell efficiency. The losses due to the contact fingers are very clearly observed in the line scan shown in Fig. 6.3. It can be noted that the general shape of the fingers stays the same throughout the solar cell.

The defect labelled **A** on the LBIC maps could be due to a localised impurity or surface defect. The defect reduces current generation, which is clearly seen in the scans. Fig 6.3 shows the line scan taken across the cell at I_{sc}, at the position indicated by the line in Fig. 6.2. The extent of the defect (**A**) can be seen when compared to the decrease in current because of the fingers. This defect negatively impacts the current generation of the solar cell and is therefore detrimental to the performance of the device.
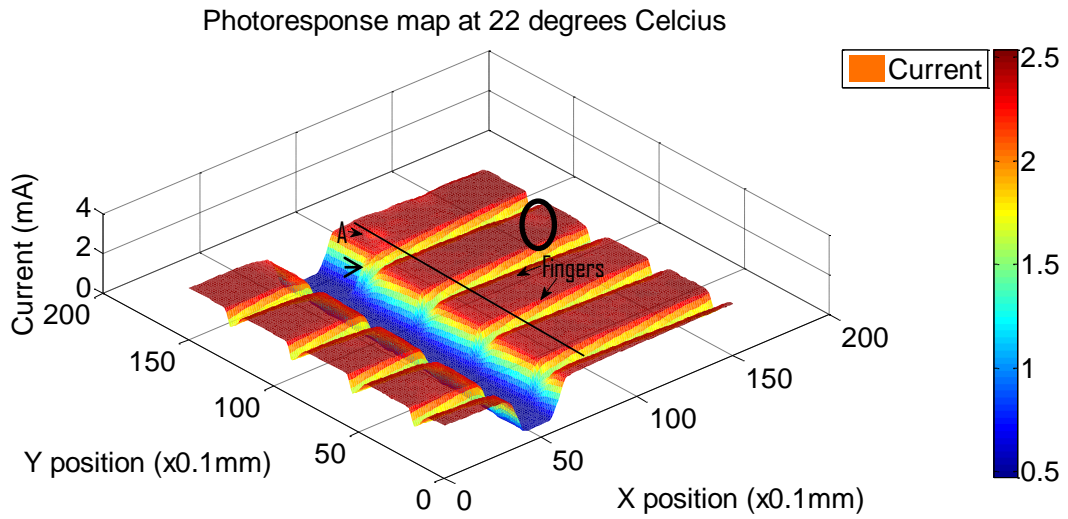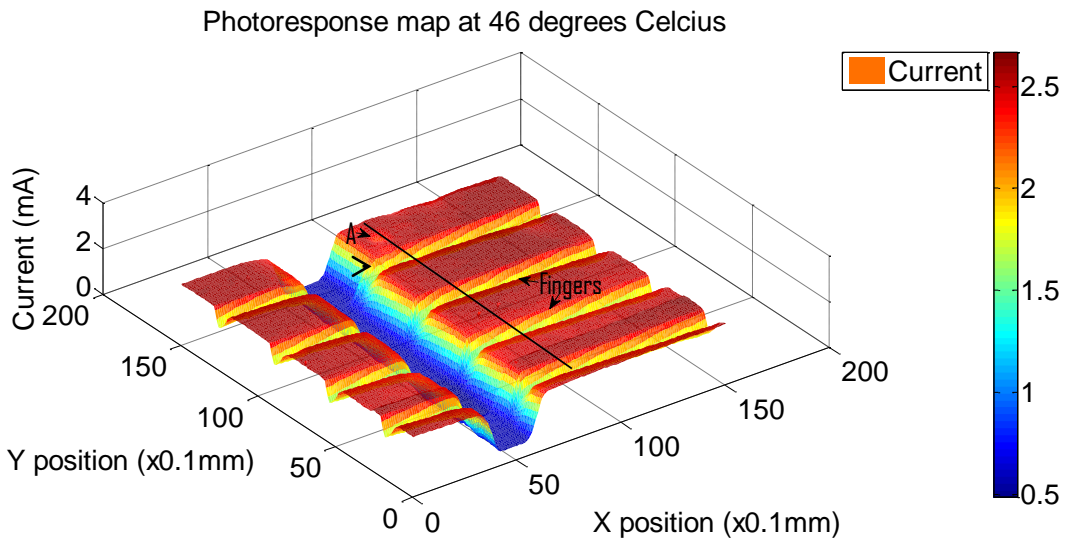
Figure 6.1: LBIC map of cell area 15.0 x15.0 mm^2 at 22 °C

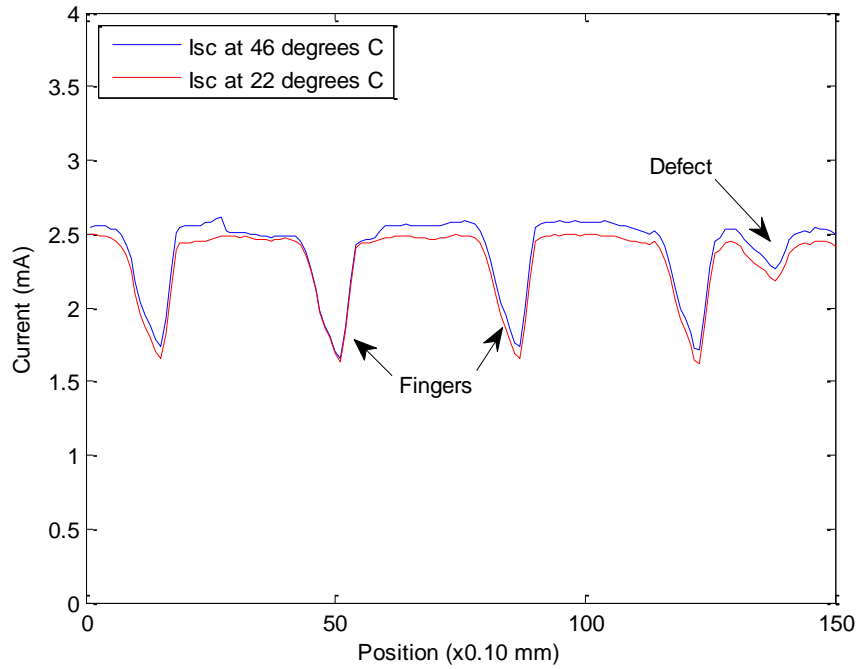**Figure 6.2:** LBIC map of cell area 15.0 x15.0 mm^2 at 46 °C

Figure 6.3: Line scan extracted across the c-Si solar cell indicated by the lines in Figures 6.1 and 6.2

6.2.1 Effect of temperature

An increase in the solar cell temperature gives rise to an increase in the energy of the charge carriers in the semiconductor material and therefore lowers the energy needed to break the bonds. This effectively reduces the bandgap energy of the material and thus affects the semiconductor material parameters. One of the parameters most affected is V_{oc}, since it is a function of the saturation current which depends on the charge carrier density of the material, and which increases with an increase in temperature [11]. This overall effect decreases the V_{oc} of the solar cells. Temperature also affects I_{sc}, as seen in in Fig. 6.3. As temperature increases, the number of photons with enough energy to create electron-hole pairs increases. The combined effect due to an increase in temperature results in a decrease in the fill factor and therefore a decrease in efficiency.

The effect of temperature on the solar cell performance can be seen in the LBIC maps in Figures 6.1 and 6.2, and it is very clear from the line scan in Fig. 6.3. It is clearly seen from the LBIC maps and line scan that the induced current increases with an increase in temperature. The current distribution across the cell is the same for both temperature ranges and is uniform.

6.2.2 Parameter extraction and mapping

Figures 6.4 to 6.11 show the parameter maps extracted using the gradient-descent optimisation (GD) algorithm and Differential evolution (DE) algorithm for the solar cell obtained using LBIC at 22°C. A noticeable feature found on most of the maps is close to the edge of the cell. There is a variation in the photo-response at the edges. The edges are areas where shunts are likely to occur and therefore contributing to edge shunting [9]. The cause of this edge effect could be due to the insufficient separation of the diffused emitter from the back contacts induced while manufacturing [1].

In addition to this performance degrading effect is the defect indicated by the circle on the maps, this defects occurs on most of the maps and is shown by the circle on the photoresponse map in Figure 6.1. This defect could be due to the inherent semiconductor material property and will be investigated further by looking at the I-V curves at specific points.

Figures 6.4 and 6.5 shows the diode ideality factor maps extracted using the GD and DE algorithms respectively described in chapter 5. The maps show noticeable changes at the circled areas and near the edges of the solar cell. The ideality factor is an indication on the performance of the solar cell device and increase in the uniformity of it will result in the device behaving poorly, thus it is expected that at these regions the efficiency of the device dropped.
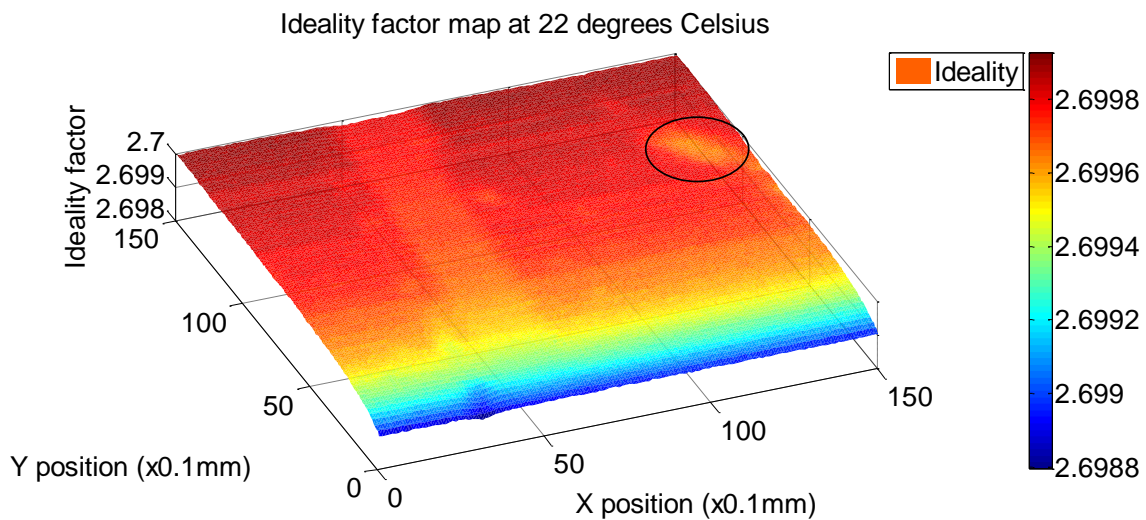

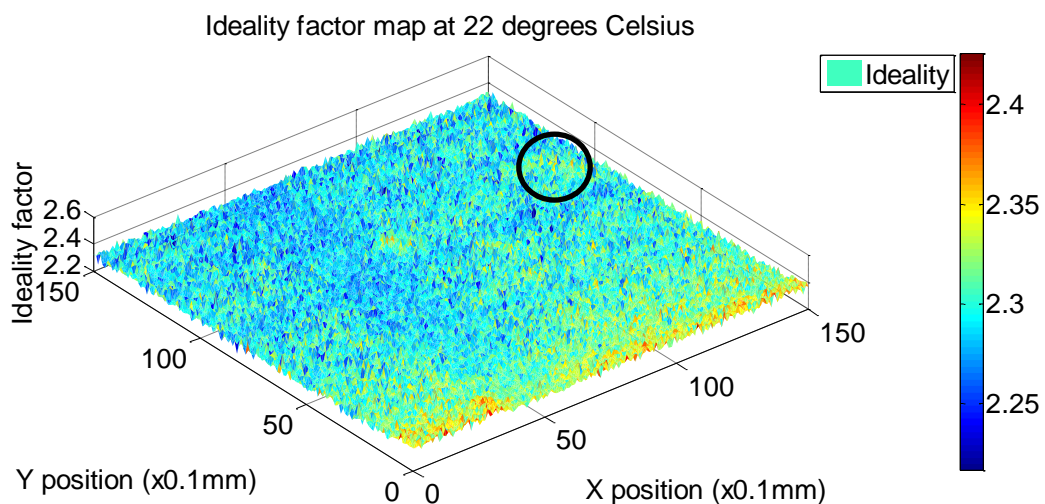**Fig 6.4:** Ideality map obtained using GD

Fig 6.5: Ideality map obtained using DE

Figures 6.6 and 6.7 indicate the saturated current maps. The order of the saturation current extracted using both algorithms are of 10^{-5} and 10^{-6} A, which results in fairly good

correspondents. The same defects are observed for both maps especially the circled area since its effect is greater on the solar cell performance.
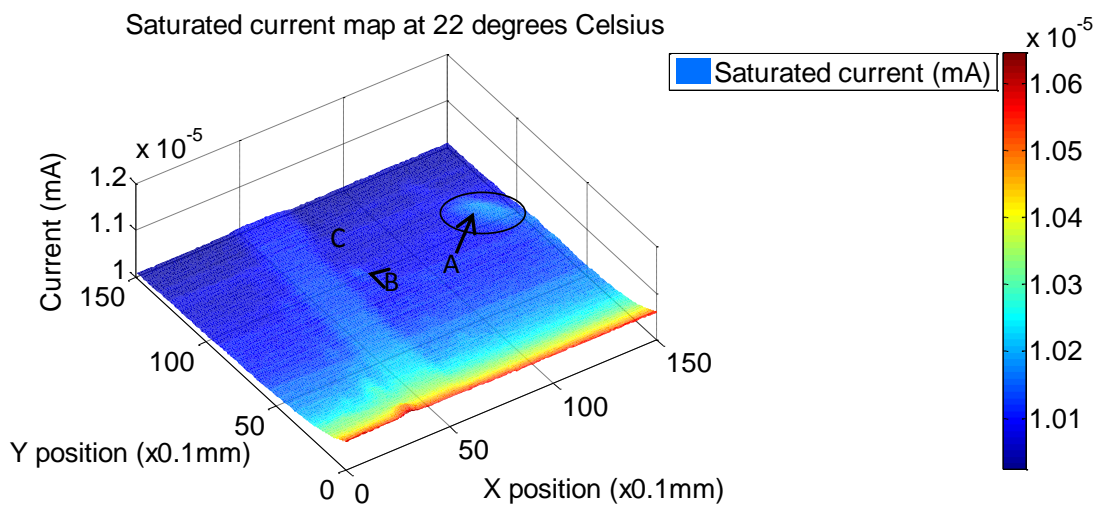

Fig 6.6: Saturated current map obtained using GD
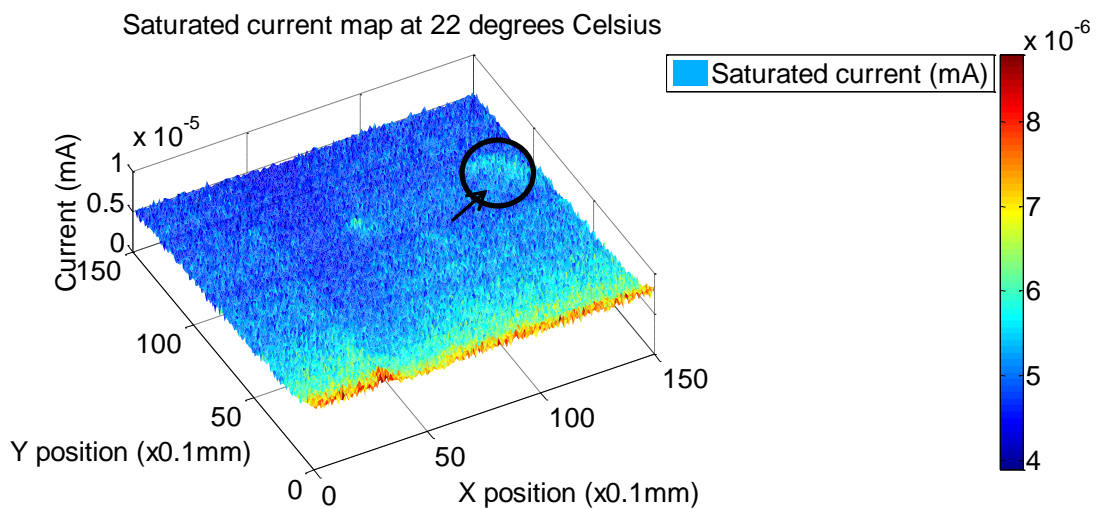
Fig 6.7: Saturated current map obtained using DE

A decrease in the shunt resistance is detrimental to solar cell performance, since this creates shunt paths across the p-n junction, which leads the charge carriers away from its intended direction. Localized areas of a decrease in the shunt resistance can clearly be observed in figure 6.8 and 6.9 and are indicated by the arrows. There is a substantial drop in the shunt resistance at the edge of the solar cell, where the edges of solar cells are known to be one of the areas where shunts are likely to occur and therefore contributing to edge shunting [9].
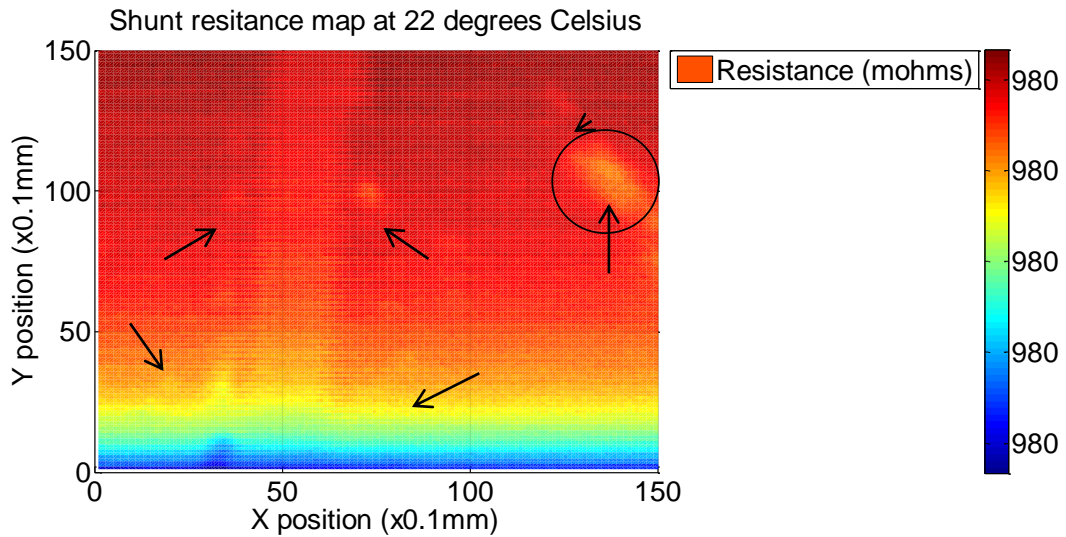
Fig 6.8: Shunt resistance map obtained using GD

Fig 6.9: Shunt resistance map obtained using DE

Figures 6.10 and 6.11 show the series resistance map of the solar cell, from these figures it is seen that there is a uniform distribution of the series resistance across the solar cell. Both algorithms shows no significant change in the series resistance, except in figure 6.11 (Differential evolution) indicated by the circled region.
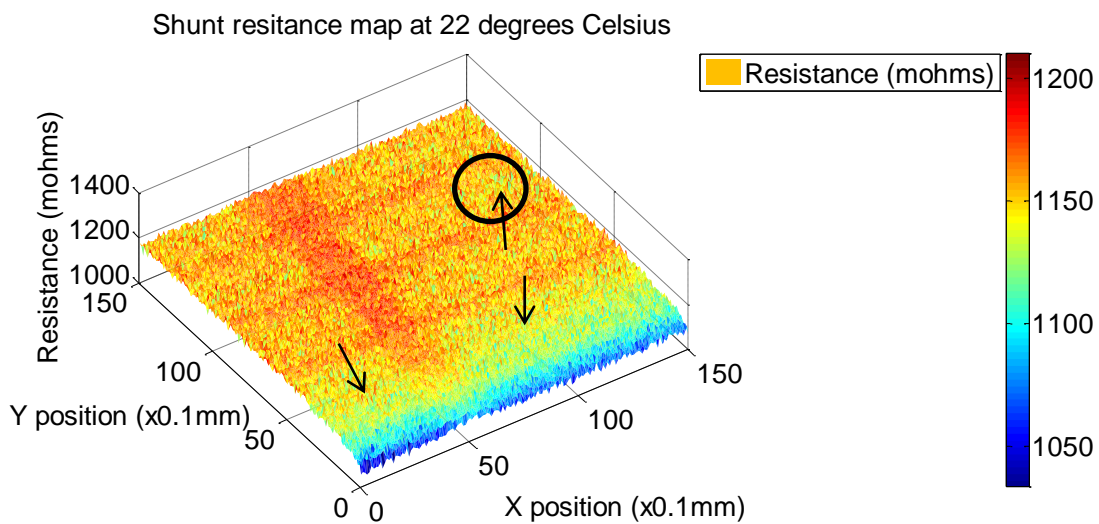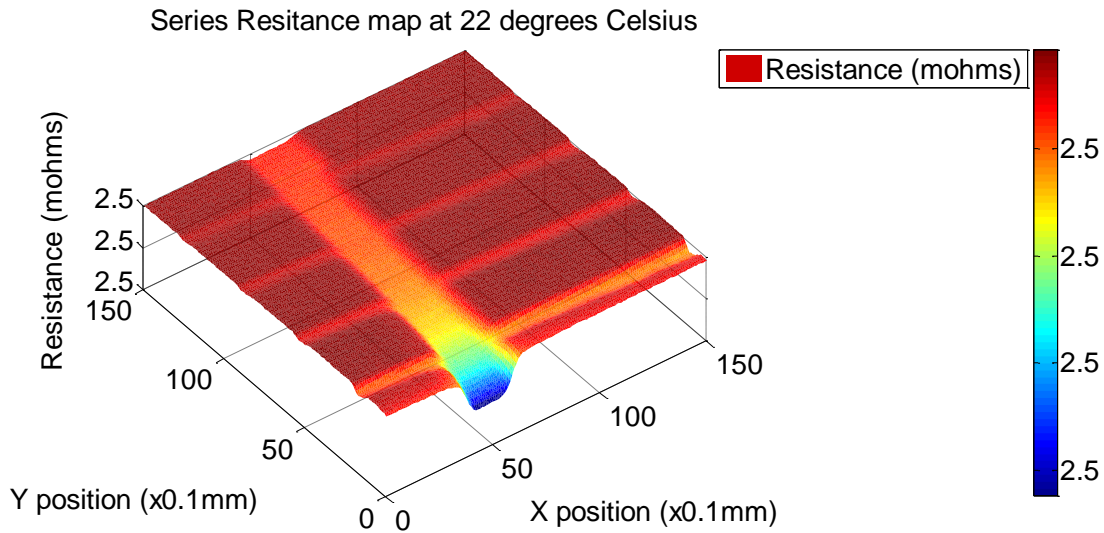
Fig 6.10: Series resistance map obtained using GD
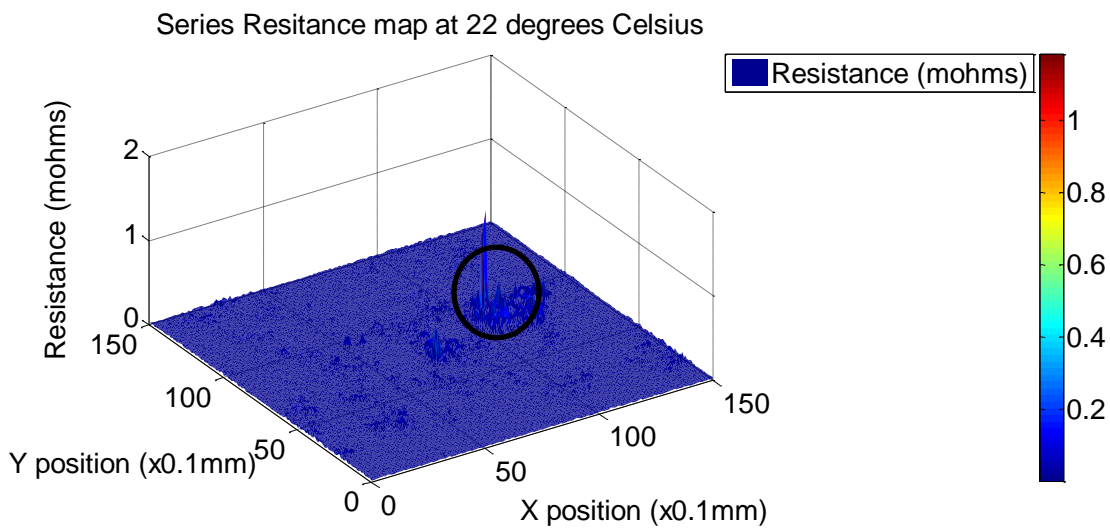
Fig 6.11: Series resistance map obtained using DE

Figures 6.12 and 6.13 shows the I-V curves of the points A, B and C indicated on figure 6.6. The figures shows the experimental and simulated results. From these curves a clear distinct variation in the I-V characteristics of regions A, B and C is seen. Region A has a much lower I_{sc} and V_{oc} compared with B and C, it is therefore expected that regions A and B will have a lower power output compared to that of C. The device parameters listed in table 5.1 and 5.2 were extracted using the gradient descent optimization algorithm and differential evolution, respectively.

The lower voltage region of the I-V curves are influenced by R_{sh} and the higher voltage region by R_s. Table 5.1 shows that these values differ slightly and this could be due to manufactured induced defects or the impurities present in the bulk of the material at these regions, which reduces the photo-generated current. The lower R_{sh} value is indicative of an

increase of shunt paths across the p-n junction of the cell, which leads the photo-generated current away from its proposed direction, thus we expect the performance of regions A and B to be less than regions C. The device parameters, n and I_0 are also listed in the tables, these have fairly similar values for all the regions. Region A reveals a higher ideality factor, although all three have n> 2, implying the junction at this region behaves poorly compared to the other regions, where region A comparatively shows slightly better behaviour. The saturation current for all is in the order of 10^{-5} A having the highest value. Analysing the numbers for the parameters extracted it confirms that regions A and B will perform weaker as to compared to region C.

Fig 6.12: I-V curve of the areas A. B and C indicated on Figure 6.6 obtained using GD model.

Table 5.1: Device performance parameters of a c-Si solar cell extracted using GD.

Region	I_L (mA)	n	R_{sh} (Ω)	R_s (Ω)	I_0 (mA)
A	2.417	2.700	979.995	2.500	1.018×10^{-5}
B	2.434	2.699	979.997	2.500	1.013×10^{-5}
C	2.476	2.667	980.000	2.498	1.005×10^{-5}

Figures 6.13 and Table 5.2 shows the I-V curves and parameters extracted of the points A, B and C indicated on Figure 6.6 using the Differential evolution model. As discussed in section 6.2.1 and confirmed by Figure 6.13 and Table 5.2 that the power out hence efficiency of points A and B will be less than point C.
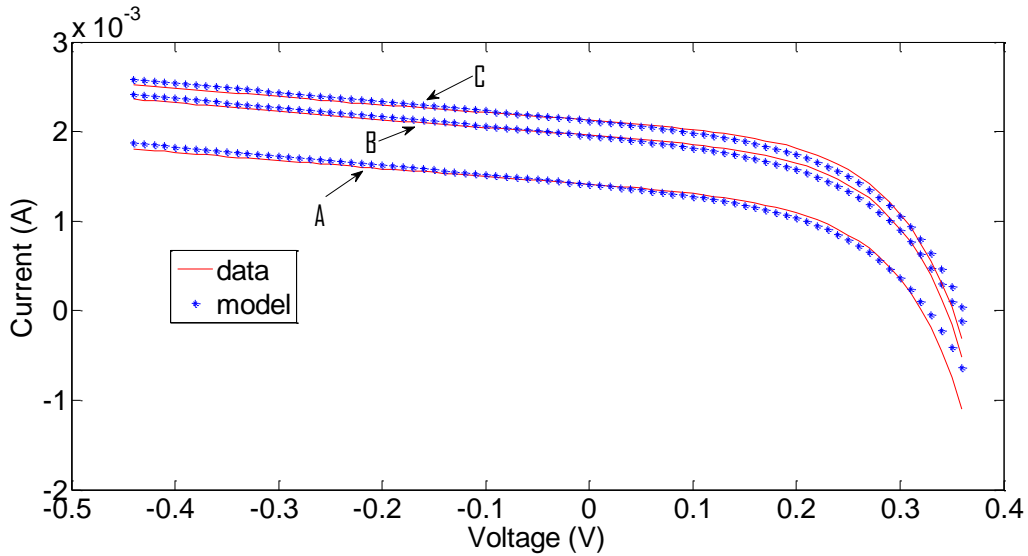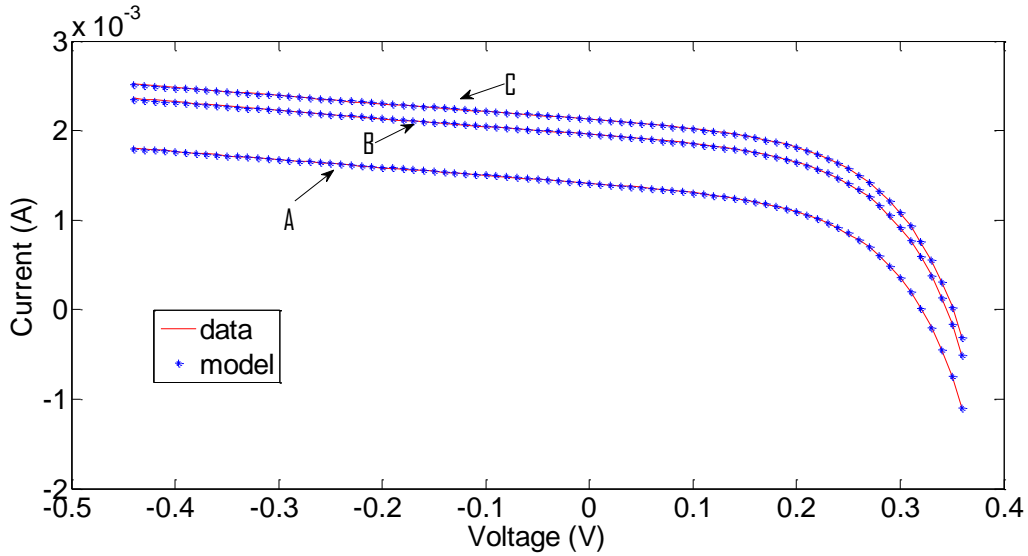
Fig 6.13: I-V curve of the areas A. B and C indicated on Figure 6.6 obtained using DE model.

Table 5.2: Device performance parameters of a c-Si solar cell extracted using DE.

Region	I_L (mA)	n	R_{sh} (Ω)	R_s (Ω)	I_0 (mA)
A	2.417	2.315	1156	0.007	5.550×10^{-6}
B	2.434	2.319	1147	0.006	5.370×10^{-6}
C	2.476	2.296	1158	0.014	4.800×10^{-6}

6.3 LBIC analyses on Multi crystalline Silicon solar cells.

LBIC was done on two different m-c Si solar cells namely a 12.0 x 12.0 mm² and 20.0 x 20.0 mm², respectively. The LBIC scans were done using a 633 nm wavelength laser beam with a spot size of approximately 100 μm incident on the cell and 100 μm step size. Similarly as discussed in section 6.1 the scans indicates the metal contacts for current collection that acts as shading features. Since the main purpose of the scans was for parameter extraction, a relatively larger spot size was required to obtain good I-V curves and this resulted in the grain boundaries not being visible on the scans. Figure 6.14 indicates the variation of the I_{sc} across the solar cell, which is clear indication of the non-homogeneity of the material of the silicon solar cell [22]. One area on the cell that is of true interest is the scratches indicated by the arrows on the LBIC scan.

The scratch induced either while manufacturing or handling of the cell, shown by the arrows in figure 6.14 produces a conductive path across the p-n junction of the solar cell, that leads current away from its intended direction, these types of induced shunt paths, decreases the overall shunt resistance of the cell and therefore reducing the performance of the device [6].

The fluctuation in the current throughout the solar cell is due to grain boundaries, which act as trapping mechanism for the majority carriers and decrease the carrier lifetime and, therefore, decreasing the efficiency of the cell. The solar cell shows an overall good response, other than the scratches and the small defects indicated by the dash arrows, which are most likely due to the multi-crystalline nature of the material.
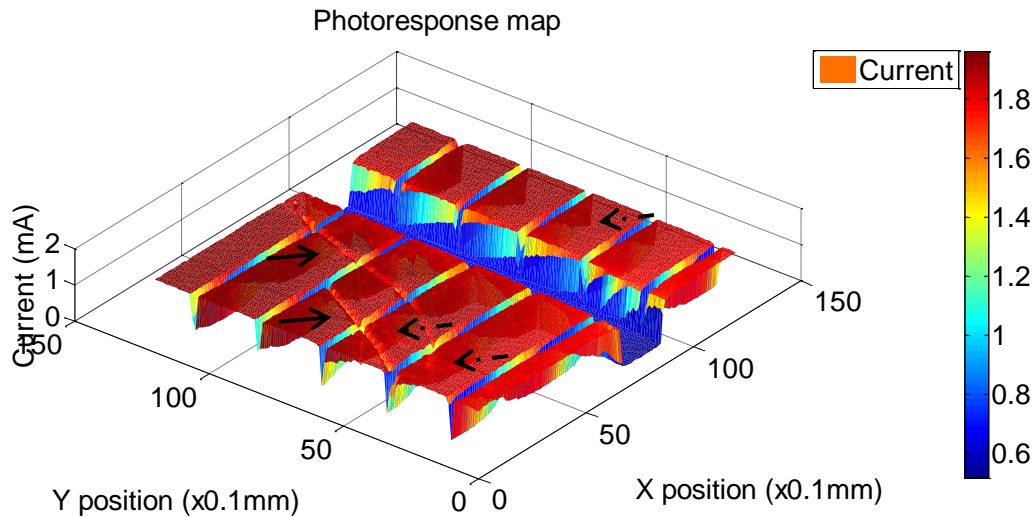

Fig 6.14: LBIC map of cell area 12.0x12.0 mm^2 at 28°C

6.3.1 Parameter extraction and mapping

Figures 6.15 to 6.22 show the parameter maps extracted using the gradient descent optimization algorithm and differential evolution methods. From these figures the contact fingers and the bus bar are clearly seen. The fairly noticeable scratches indicated by the arrows are observed on most of the maps known to be one of the areas where shunts are likely to occur and therefore contributing to poor performance [9].

The ideality factor which is an indicator of the quality of the diode varies throughout the cell, where noticeably it's higher at the metal contacts than that of the semiconductor material which is what is expected due to the non-semiconductor properties at these contacts. An increase in the ideality factor is an indicator of diode behaving poorly and therefore the performance of the device dropping. Recombination in the space-charge region leads to 1<n<2, while recombination in the bulk of the material leads to n>2, which is observed using both methods to determine the mapping of n as seen in figures 6.15 and 6.16
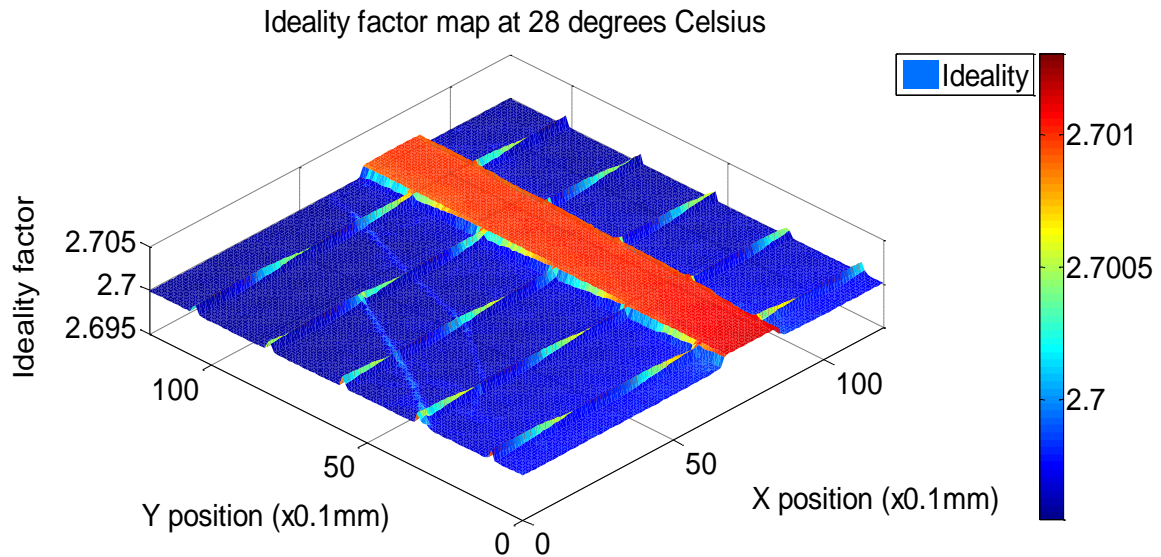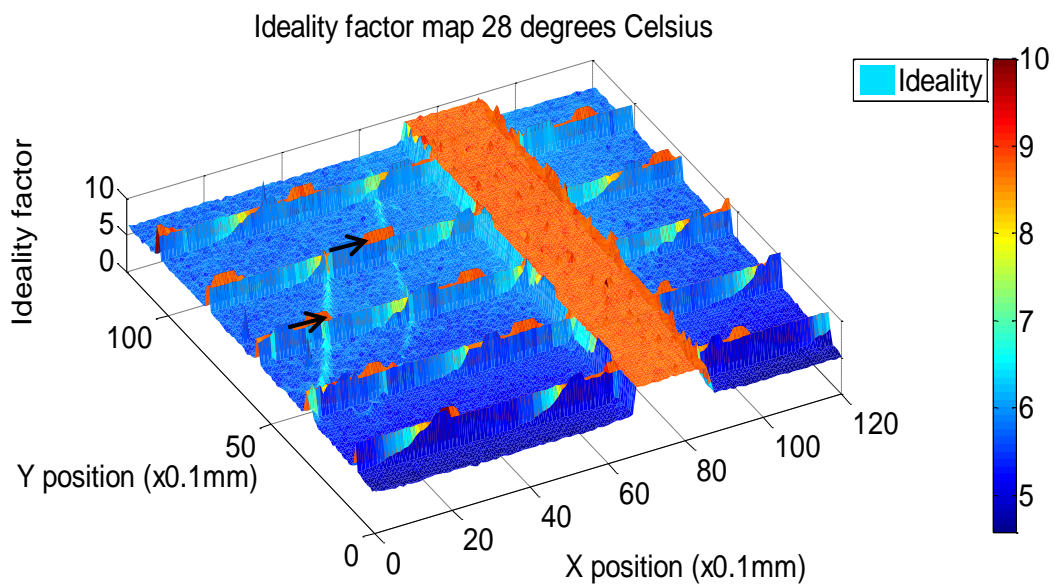
Fig 6.15: Ideality map obtained using GD

Fig 6.16: Ideality map obtained using DE

For an ideal solar cell a high shunt resistance is required, a low shunt is indicative of an increase in the shunt paths across the semiconductor p-n junction, these shunts paths lead current away from their intended direction and hence decreasing the performance of the solar cell [1]. Shunts are dominant in m-c Si compared to c-Si due to the inhomogeneity of the crystal structure [13]. From figures 6.17 it is seen that there is a decrease in the shunt resistance in the region by the scratches which is a result of the shunt paths created and also the top quarter indicated by the double headed arrow of the solar cell near the edge. The edges of solar cells are known to be one of the areas where shunts are likely to occur

and therefore contributing to edge shunting [9]. It is furthermore noticed that the DE technique is not sensitive to the small variation in R_{sh} observed by the GD technique.

Shunt resitance map at 28 degrees Celsius
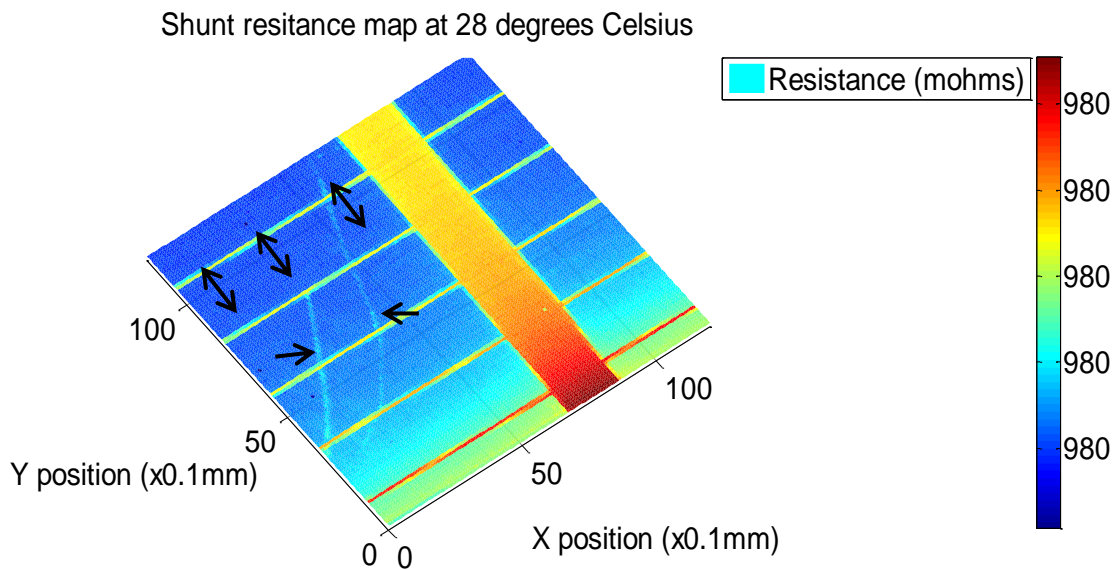
Fig 6.17: Shunt resistance map obtained using GD.

Shunt resitance map 28 degrees Celsius
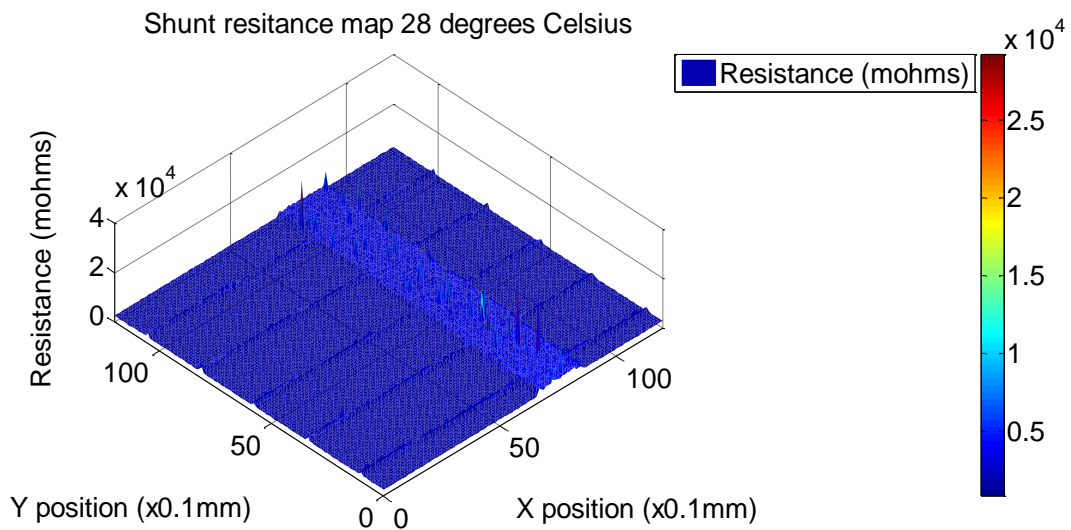

Fig 6.18: Shunt resistance map obtained using DE.

The series resistance maps indicated by figures 6.19 and 6.20 shows a slight variation throughout the solar cell except at the scratches. The distribution of this variation is most likely due to doping non-uniformity since the resistivity of the device is a function of the doping concentration of the material [9].
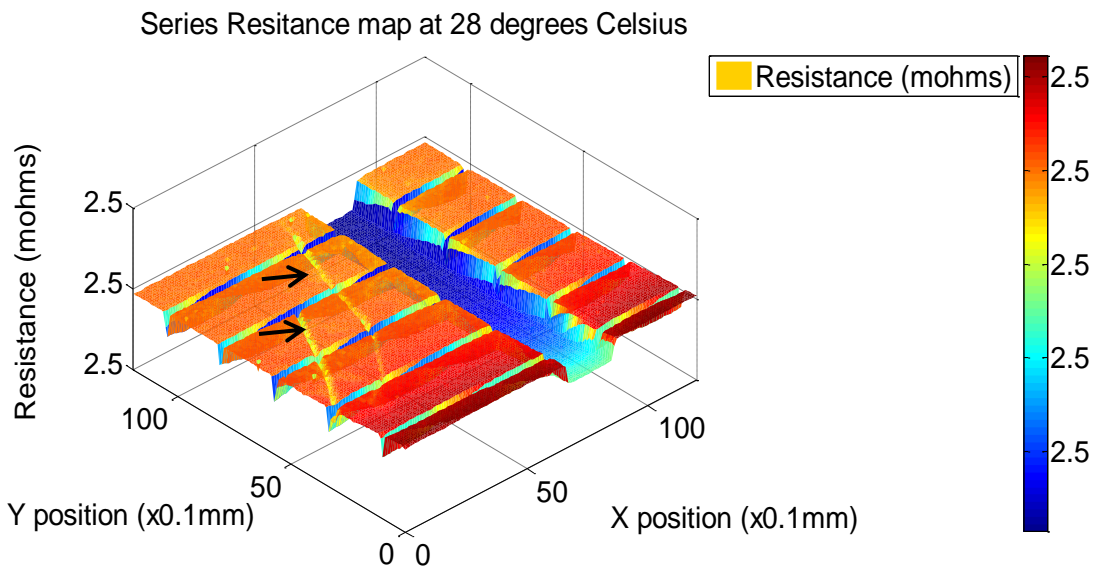
Fig 6.19: Series resistance map obtained using GD
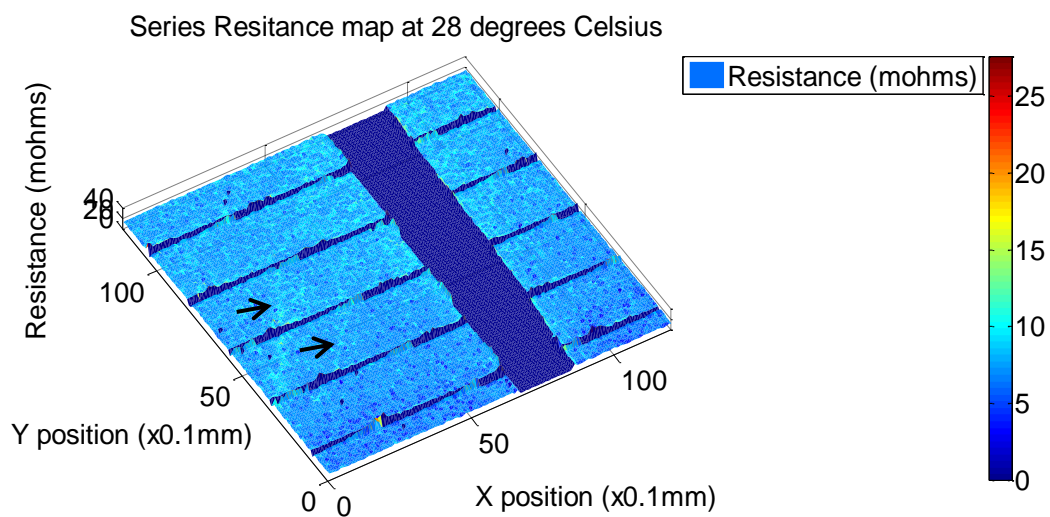
Fig 6.20: Series resistance map obtained using DE

Like the Ideality factor the saturation current depends on the material quality and is affected by the carrier mobility and diffusion lengths. Defects present in the semiconductor material leads to high recombination which in tandem leads to a high saturation current. From figures 6.21 and 6.22 it is seen that regions where the scratch occur results in a lower saturation current, thus verifying that the scratch is detrimental to the solar cell performance.

The overall increase in the saturation current and ideality factor suggest an increase in recombination, this effect coupled with an increase series resistance and decrease in shunt resistance lowers the fill factor of the device and hence the efficiency.

Fig 6.21: Saturated current map obtained using GD.
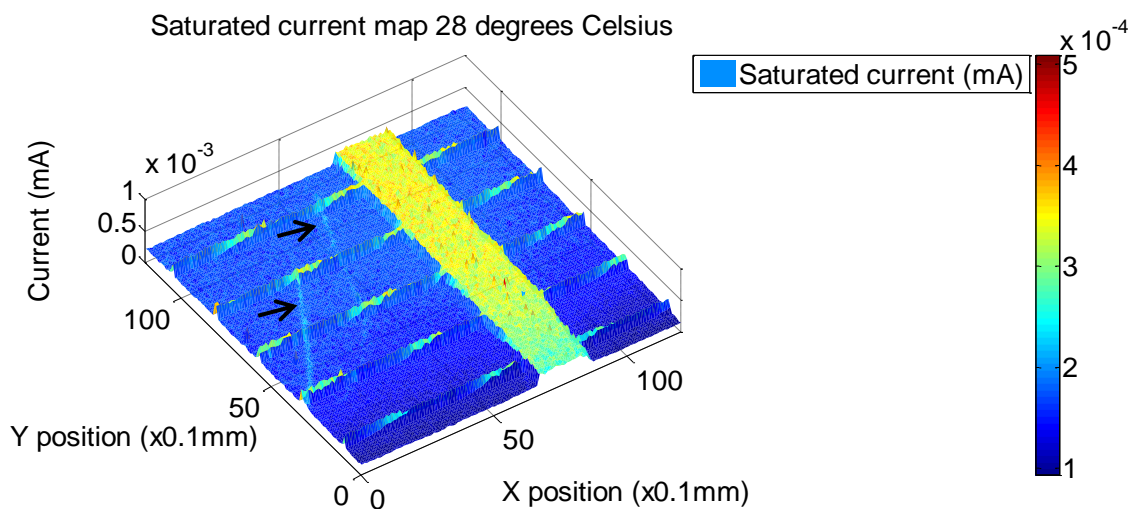
Fig 6.22: Saturated current map obtained using DE.

6.3.1.2 Comparison of the models.

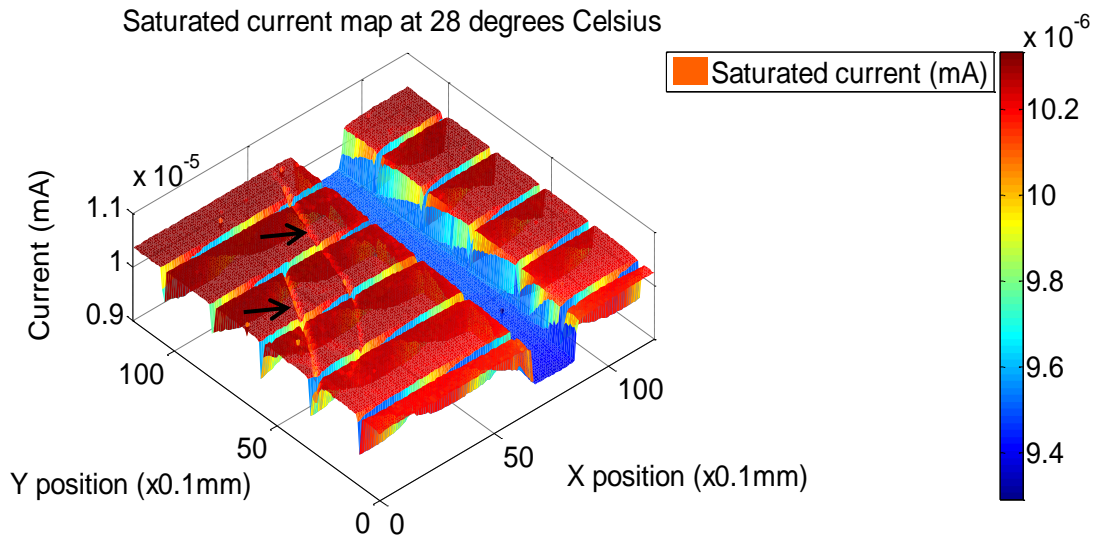The device parameters extracted vary slightly for the two models. The fitness of the error for the gradient descent algorithm was of the order 10^{-7} whereas for the differential evolution it was of the order 10^{-9}, which is an indication that the differential evolution is slightly more accurate than the gradient descent. The time duration for running the gradient descent algorithm is on average 50 minutes more than running the differential evolution for the same data set.

6.3.2 Temperature effect on the performance of an m-c Si solar cell.

As discussed in section 6.2.1 an increase in temperature results in a decrease in V_{oc} and an increase in I_{sc}. Figures 6.23 and 6.24 show the LBIC maps of the 20mm x 20 mm multi crystalline silicon solar cell at 27 °C and 33.7°C respectively. The scans show the fingers

and busbars, the variation in the I_{sc} across the cell for both scans are fairly constant and the slight variation that might occur would mainly be due to the non-uniformity of the crystal structures.

Figure 6.25 shows the line scan across the area indicated on the photoresponse maps at I_{sc}. The line scan clearly indicates the photo generated current induced under illumination and the current reducing features i.e fingers and defects. The defects is mainly due to impurities in the material, however could be surface defects. To determine whether it is surface defects, reflection mapping needs to be done and is not in the scope of the project. From this figure it is seen that the magnitude of the LBIC signal decreases with an increase in temperature, more noticeably the defect indicated by the circle on Fig 6.25, for lower temperatures is almost as great as that of the fingers compare to that of the same defect at the higher temperature. This could be due to the injection level increasing at higher temperature, thus more interaction between the charge carriers.
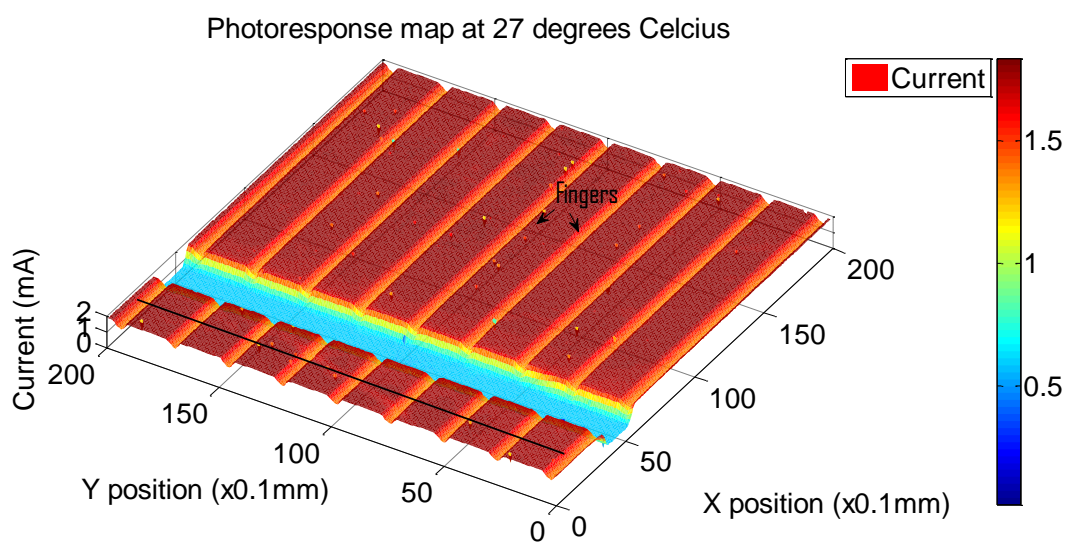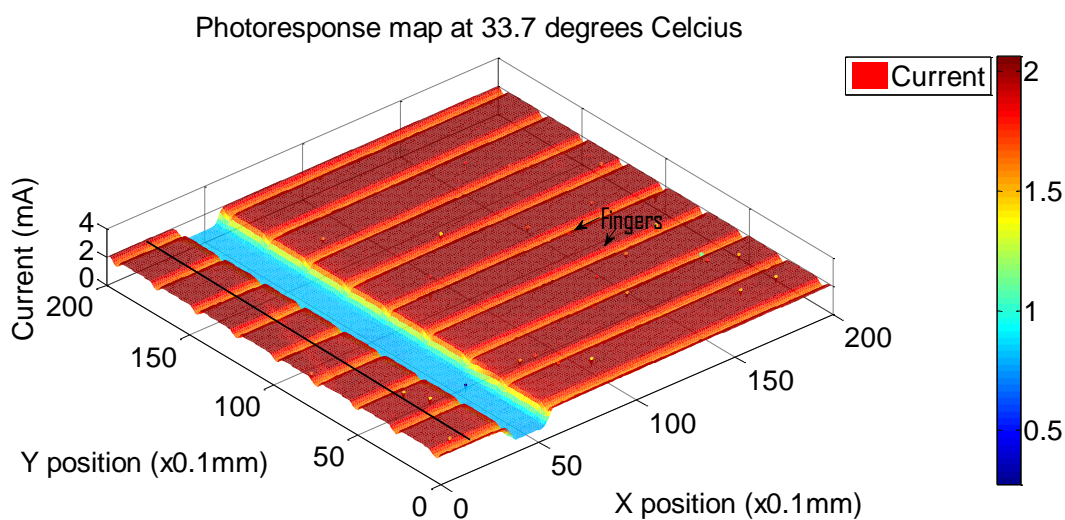

Fig 6.23: LBIC map of cell area 20.0x20.0 mm^2 at 27 °C.

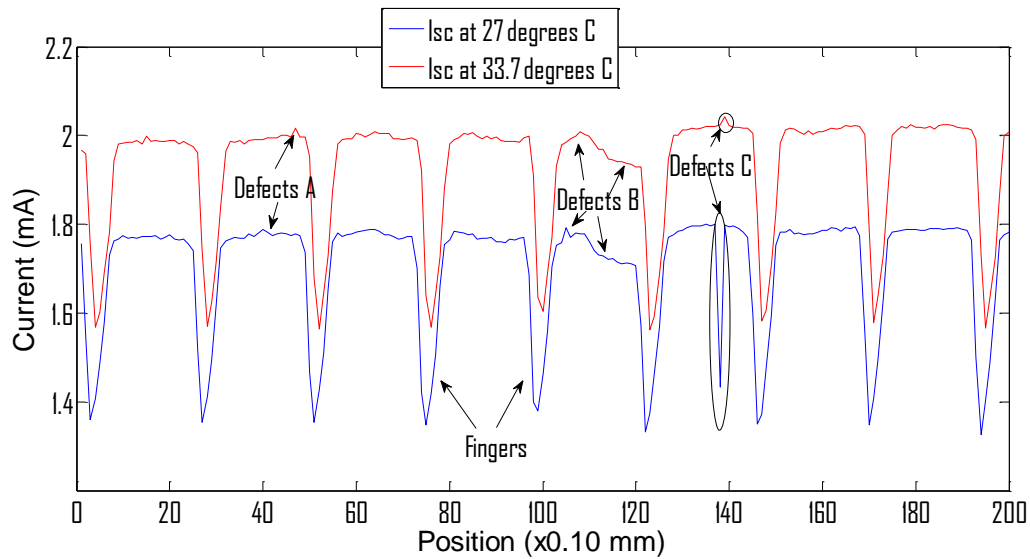**Fig 6.24**: LBIC map of cell area 20.0x20.0 mm^2 at 33.7 °C.

54

Fig 6.25: Line scan extracted across the c-Si solar cell indicated by the lines in figures 6.23 and 6.24.

At higher temperatures the short circuit current increases slighty since the band gap energy decreases and more noticeably the open circuit voltage decreases as discussed in the previous sections. These two effects combined reduce the fill factor and hence the efficiency, thus an increase in temperature is detrimental to the performance of the solar cell device.

6.4 Summary

The LBIC system designed and constructed is a non-destructive diagnostic tool that allows for the identification and characterisation of the defects in solar cells. LBIC measurements and I-V characteristics measured for single and multi-crystalline silicon solar cells, the I-V characteristics of the cells was used for the extraction of device parameters using two techniques; Gradient descent optimization algorithm and the Differential evolution algorithm.

In the first part of the chapter, LBIC measurements of a c-Si solar cell at different temperatures were obtained. The results indicated the overall effect of an increase in temperature on the I_{sc} and V_{oc}, which contributed to a drop in the solar cell efficiency. The resulting cell data was subjected to the DE and GD algorithms for the extraction of device parameters. The parameters obtained from the models showed the effect of different device parameters on the performance of the solar cell.

In the second part, m-c Si solar cells was subjected to LBIC measurements. The LBIC photoresponse maps indicated scratches and defect regions that were detrimental to the performance of the device. The solar cell was subjected to the two parameter extraction models and the effect of the scratches, industrial induced defects and impurities within the material was observed on the parameters.

55

In addition the effect of temperature on m-c Si solar cell was investigated. The results yielded an increase in the photoresponse at higher temperatures. The overall effect of an increase in temperature results in a decrease in the efficiency of the device.

Chapter 7: Conclusion

The main objective of this study was to design and construct an LBIC system for the characterisation of solar cells in order to identify performance limiting defects present in the semiconductor material. The LBIC system that was constructed is able to map the photo-response of a solar cell as a function of position across the cell. In addition, by biasing the solar cell at pre-determined voltages between reverse and forward bias, the I-V characteristics may be obtained at predetermined points on the cell. These point-by-point I-V characteristics allowed for the extraction of the solar cell parameters across the solar cell.

The other main objective of this study was the development of a parameter extraction algorithm, known as Gradient-Descent Optimization, which was created to electrically characterise the solar cells from the I-V characteristics. A complementary technique known as Differential Evolution was also used.

The operation of the LBIC system and application of the parameter extraction algorithms were demonstrated by investigating two different solar cell technologies, viz. c-Si and mc-Si. LBIC maps of both solar cells were obtained at different temperatures to observe the effect of temperature on the behaviour of a solar cell. From the results obtained, it was concluded that an increase in temperature leads to an increase in the short-circuit current and a decrease in the open-circuit voltage. The combined effect of these factors acts to reduce the performance of a device and therefore decrease its efficiency. The LBIC maps also clearly showed different current reducing features, such as scratches and edge effects on the solar cell, which showed the negative impact on the performance of the cell.

From the I-V characteristics obtained, the performance parameters were extracted using the two algorithms mentioned. The effect of the different parameters on the performance of the solar cell was observed. The sum squared error of the model to the data for both algorithms was 10^{-7} and 10^{-9} for gradient-optimisation and differential evolution, respectively, which resulted in the algorithms yielding accurate maps.

The study highlighted the importance of LBIC as a non-destructive tool for identifying and characterising defects within the solar cells. The I-V characteristics obtained were also a useful tool for electrical characterisation of the solar cells, and helped to create a better understanding of the behaviour of the device parameters.

Chapter 8: References

1. S. Hegedus A. Luque. Handbook of Photovoltaic Science and Engineering. Wiley, 2002.

2. N. W. Ashcroft, N. D. Mermin, Solid state physics. (Brooks/ Cole Cengage learning)

3. R.J. Overstraeten. R. P Mertens, Physics, Technology and Use of Photvoltaics. (Adam HilgerLTD, Bristol, 1986).

4. M.A. Green, *Solar Cells.* (Artech House, Boston, 1992).

5. P. Wurfel, Physics of solar cells, from principle to New Concepts. (WILEY-VCH Verlag GmbH & Co. KGaA, 2005)

6. D. N. Wright, Optical and passivating properties of hydrogenated amorphous silicon deposited by plasma enhanced chemical vapour deposition for application on silicon solar cells. PHD. Thesis. 2008.

7. N. M. Thantsha, Spatially Resolved opto-electrc measurements of photovoltaic materials and devices. PHD. Thesis, Nelson Mandela Metropolitan University (2010).

8. Principle and Varieties of Solar Energy and Fundamentals of solar cells, The University of Toledo, Department of Physics and Astronomy. February 2012.

9. M.K Munji, Characterisation of concentrator solar cell devices and materials using Light-Beam Induced Current measurement., PHD. Thesis, Nelson Mandela Metropolitan University (2011).

10. J. L. Crozier, Investigation into cell mismatch in photovoltaic modules. MSc. Thesis, Nelson Mandela Metropolitan University (2012).

11. C. Hosenberg, S Bowden. PV CDRom, (Accessed on 13/06/2013). http://pveducation.org/

12. E. Q. B. Macabebe, Investigation of device and performance parameters of photovoltaic devices. PHD. Thesis, Nelson Mandela Metropolitan University (2009).

13. A.R, Gxasheka. On the optical characterisation of photovoltaic devices, PHD. Thesis, Nelson Mandela Metropolitan University (2008).

14. J. Sites, T. Nagle, LBIC analysis of thin-film polycrystalline solar cells. Physics Department, Colorado State University, Fort Collins, CO 80523.

15. Edmund optics Beam expander maunual, 2012. www.edmundoptics.com

16. Micos Motion control and Optics SMC motor and controller manual

17. Stanford Research Systems SR570 manual, 2005.

18. The National Instruments USB-6356 data acquisition system manual.

19. R. Storn, K. Price, Differential Evolution - A simple and efficient adaptive scheme for global optimization over continuous spaces. International Computer Science Institute. 1996.

20. MC. Du Plessis, Adaptive multi-population differential evolution for dynamic environments. PHD. Thesis, University of Pretoria (2012).

21. Goetzeberger A., Knobloch J., Voss B., *In Crystalline Silicon Solar Cells*. John Wiley, Chichester, (1998), pp. 84-85.

22. Ibrahim, A., *LBIC Measurements Scan as a Diagnostic Tool for Silicon Solar Cell.* Textroad Publications, (2010).

References not cited directly

1. F. J. Voster, On the characterisation of photovoltaic devices for concentrator purposes. PHD. Thesis, Nelson Mandela Metropolitan University (2007).

2. S. Bremmer, Solar electric systems, University of Delaware. 2009

3. B.Moralejo, M.A Gonzalez, J. Jimemez, V. Parra, O. Martinez, J. Gutieprez and O Charro. LBIC and reflectance Mapping of Multicrystalline Si solar cells. Journal of Electronics materials, Vol. 39, No 6, 2010.

4. Mathematica, Method of Steepest descent. (Accessed on 20/10/2013). http://mathworld.wolfram.com/MethodofSteepestDescent.html.

5. E.L. Meyer, E.E. van Dyk, "Assessing the reliability and degradation of PV module performance parameters", (IEEE Transactions on Reliability, 53, No.1, March 2004).

6. J. Marek, " Light-beam-induced current characterisation of grain boundaries," Journal of Applied Physics 55, 318-326(1984)

7. N. M. Thantsha, E. Q. B. Macabebe, F. J. Vorster, and E. E. van Dyk, "Optoelectronic analysis of silicon cells by LBIC investigation and current-voltage characterization," Physica B 404, 4445–4448 (2009).

Appendix A

Research outputs associated with this work

National Conferences Attended

- Annual South African Institute of Physics conference 2012.

- Annual Centre for Renewable and Sustainable 2012

- Annual South African Institute of Physics conference 2013.